Upward transport into and within the Asian monsoon anticyclone as inferred from StratoClim trace gas observations

Marc von Hobe[1], Felix Ploeger[1,5], Paul Konopka[1], Corinna Kloss[1,2], Alexey Ulanowski[3], Vladimir Yushkov[3], Fabrizio Ravegnani[4], C. Michael Volk[5], Laura L. Pan[6], Shawn B. Honomichl[6], Simone Tilmes[6], Douglas E. Kinnison[6], Rolando R. Garcia[6], Jonathon S. Wright[7]

[1]Institute for Energy and Climate Research (IEK-7), Forschungszentrum Jülich GmbH, 52425 Jülich, Germany
[2]Laboratoire de Physique et Chimie de l'Environnement et de l'Espace (LPC2E), Université d'Orléans, CNRS, Orléans, France
[3]Central Aerological Observatory, Dolgoprudnyi, Moscow region, Russia
[4]CNR Institute of Atmospheric Science and Climate (ISAC), I-40129 Bologna, Italy
[5]University of Wuppertal, Institute for Atmospheric and Environmental Research, Wuppertal, Germany
[6]National Center for Atmospheric Research (NCAR), POB 3000, Boulder, CO, 80307, USA
[7]Department of Earth System Science, Tsinghua University, Beijing 100084, China

Correspondence to: Marc von Hobe (m.von.hobe@fz-juelich.de)

Abstract. Every year during the Asian summer monsoon season from about mid-June to early September, a stable anticyclonic circulation system forms over the Himalayans. This Asian summer monsoon (ASM) anticyclone has been shown to promote transport of air into the stratosphere from the Asian troposphere, which contains large amounts of anthropogenic pollutants. Essential details of Asian monsoon transport, such as the exact time scales of vertical transport, the role of convection in cross-tropopause exchange, and the main location and level of export from the confined anticyclone to the stratosphere are still not fully resolved. Recent airborne observations from campaigns near the ASM anticyclone edge and centre in 2016 and 2017 respectively show a steady decrease in carbon monoxide (CO) and increase in ozone (O_3) with height starting from tropospheric values of around 100 ppb CO and 30–50 ppb O_3 at about 365 K potential temperature. CO mixing ratios reach stratospheric background values below ~25 ppb at about 420 K and do not show a significant vertical gradient at higher levels, while ozone continues to increase throughout the altitude range of the aircraft measurements. Nitrous oxide (N_2O) remains at or only marginally below its 2017 tropospheric mixing ratio of 333 ppb up to about 400 K, which is above the local tropopause. A decline in N_2O mixing ratios that indicates a significant contribution of stratospheric air is only visible above this level. Based on our observations, we draw the following picture of vertical transport and confinement in the ASM anticyclone: rapid convective uplift transports air to near 16 km in altitude, corresponding to potential temperatures up to about 370 K. Although this main convective outflow layer extends above the level of zero radiative heating (LZRH), our observations of CO concentration show little to no evidence of convection actually penetrating the tropopause. Rather, further ascent occurs more slowly, consistent with isentropic vertical velocities of 0.7 - 1.5 K day^{-1}. For the key tracers (CO, O_3,

and N_2O) in our study, none of which are subject to microphysical processes, neither the lapse rate tropopause (LRT) around 380 K nor the cold point tropopause (CPT) around 390 K marks a strong discontinuity in their profiles. Up to about 20 to 35 K above the LRT, isolation of air inside the ASM anticyclone prevents significant in-mixing of stratospheric air. The observed changes in CO and O_3 likely result from *in-situ* chemical processing. Above about 420 K, mixing processes become more significant and the air inside the anticyclone is exported vertically and horizontally into the surrounding stratosphere.

1 Introduction

The Asian summer monsoon (ASM) anticyclone is the dominant large-scale circulation system in the northern hemisphere (NH) summertime upper troposphere and lower stratosphere (UTLS) (e.g. Hoskins and Rodwell, 1995). Deep ASM convection drives vertical transport of boundary layer air to the UTLS, where the confinement of anticyclonic flow facilitates a persistent chemical signature that has been detected by multiple satellite sensors (Filipiak et al., 2005; Park et al., 2008; Park et al., 2007; Randel and Park, 2006; Randel et al., 2010; Santee et al., 2017; Thomason and Vernier, 2013; Vernier et al., 2011). Randel et al. (2010) illustrated this troposphere-to-stratosphere transport using hydrogen cyanide (HCN), a tracer of anthropogenic pollution and biomass burning measured by ACE-FTS (Atmospheric Chemistry Experiment – Fourier Transform Spectrometer, installed on the Canadian satellite SCISAT), and described the ASM anticyclone as a gateway for boundary layer air from one of the most polluted areas on Earth to enter the global stratosphere while bypassing the tropical tropopause.

These satellite observations, although effective in demonstrating the seasonal-average signature, do not have sufficient space-time resolution to clarify some of the key characteristics of this transport pathway. There are a number of outstanding questions regarding the role of ASM transport in connecting Asian boundary layer emissions and regional pollution to global tropospheric and stratospheric chemistry, and to the ensuing perturbations in regional and global climate. These questions include the most efficient vertical transport locations and time scales, the dynamical processes driving these transport patterns, the respective roles of deep convection and large-scale radiatively-balanced ascent, the dominant source regions for air masses that feed into the anticyclone, the extent of dynamical confinement within the anticyclone, the vertical and horizontal transport pathways of air masses exiting the anticyclone, and the quantitative impact of the ASM on stratospheric water vapour, ozone, and aerosols. These questions have been the focus of a large number of studies using chemical transport models, Lagrangian trajectory models, reanalysis products, and observational data (e.g. Bergman et al., 2013; Fu et al., 2006; Lau et al., 2018; Li et al., 2005; Li et al., 2020; Pan et al., 2016; Park et al., 2009; Ploeger et al., 2015; Ploeger et al., 2017; Vogel et al., 2015; Vogel et al., 2019; Yan et al., 2019; Yu et al., 2017; Nützel et al., 2019).

60   Of particular interest to this study is a characteristic description of the ASM transport structure that has emerged from recent modelling studies (Bergman et al., 2013; Pan et al., 2016):

I.   Although the chemical signature of uplifted tropospheric species fills the entire anticyclone in the seasonal-average view, deep vertical transport to the anticyclone level occurs primarily in a region in the southeastern quadrant of the anticyclone (consistent with the linearized model for off-equatorial convective forcing of tropical waves

65   presented by Gill, 1980), centred near the southern flank of the Tibetan Plateau and including the southern slope of the Himalayas, northeast India and Nepal, and the northern portion of the Bay of Bengal.

II.   In this preferred uplift region, transport from the boundary layer to the tropopause level behaves like a "chimney", dominated by rapid ascent.

III. This behaviour changes at the upper troposphere (UT) level, where sub-seasonal dynamics drive east-west oscilla-

70   tions of the anticyclone. These 10–to–20–day oscillations mix the uplifted boundary layer air within the large-scale anticyclone, and contribute to mixing of anticyclone air with the background, thus providing a pathway for this air to enter the global stratosphere.

The transport behaviour described in II has been supported by an analysis using Modern-Era Retrospective analysis for Research and Applications, Version 2 (MERRA-2) assimilated trace gases and aerosols (Lau et al., 2018), where the peak monsoon-season aerosol transport is described as a "double-stem-chimney cloud" structure that extends from the boundary layer

75   to around 16 km, near the tropopause level. The "double-stem" rapid convective lofting is identified over two localized areas: the Himalayas-Gangetic Plain and the Sichuan Basin in southwestern China.

This rapid uplift is of special interest for ASM research because the relatively short transport time scale makes this pathway an effective route for very-short-lived (VSL) ozone depleting substances (ODS) to reach the stratosphere. The level at which convectively-driven transport transitions to wave-driven slow ascent is among the outstanding issues that must be addressed

80   to further characterize this transport pathway and its effective time scale. Earlier studies often put this level at approximately 360 K potential temperature (e.g. Park et al., 2009) based on average tropical conditions. New satellite observations over the last decade indicate that the ASM region contains significantly deeper convection, indicated by higher frequencies of convective cloud tops above 380 K potential temperature (Ueyama et al., 2018).

Verification of the chimney-like behaviour suggested by model results requires detailed analysis of high-resolution airborne

85   measurements. The StratoClim campaign using the stratospheric research aircraft M55-Geophysica is the first airborne campaign to provide data suitable for such verification. Based out of Kathmandu, Nepal, StratoClim conducted eight research flights in the central region of the ASM anticyclone in summer 2017.

In this work, we use airborne in-situ measurements of carbon monoxide (CO), ozone (O_3), and nitrous oxide (N_2O) collected both outside and inside the ASM anticyclone, and here particularly in the vicinity of the "chimney" regions. We focus on these three trace gases because they provide complementary information on transport, mixing, and processing. CO is a tropospheric tracer that is enhanced in polluted air and experiences photochemical removal in the UTLS with a lifetime around 2 to 3 months, and is thus a suitable tracer to investigate the vertical reach of deep convection. O_3 is photochemically produced in the UTLS and above at rates as large as a few ppb per day. Concentrations of O_3 can reach ppm levels in the stratosphere but do not typically exceed a few tens of ppb in the troposphere, making it useful for examining the transition from tropospheric air to stratospheric air. N_2O is a tropospheric tracer with a significantly longer photochemical lifetime than CO, so that the two tracers can be used together to infer transport time scales. N_2O is removed only after substantial residence time within the stratosphere. Significant reductions in N_2O mixing ratios thus indicate in-mixing of aged stratospheric air.

Using these three trace gases together with dynamical variables, we address the following questions:

Q1   Does the vertical distribution of CO and O_3 support the occurrence of rapid convective transport up to the tropopause level?

Q2   At what potential temperature level does the time scale of transport change based on observed vertical gradients in the trace gas profiles?

Q3   Where is this transition region located relative to the tropopause?

Q4   At what level do we begin to see significant signatures of mixing with stratospheric air?

The flights and measurements are described in Section 2, which also introduces model tools and specific dynamical coordinates used in the analysis. Statistical analysis of the observations in terms of different horizontal and vertical coordinates and a comparison of observed and simulated O_3 vs. CO tracer correlations are presented in Section 3, followed by detailed discussion of the results in the context of the four questions listed above in Section 4. In the concluding Section 5, we draw a summary picture of vertical transport and confinement inside the ASM anticyclone and compare this to other recent studies.

2 Methods

2.1 Field campaigns

Two airborne field campaigns utilizing the high-altitude aircraft M55 Geophysica were carried out under the umbrella of the EU project StratoClim. Three flights were conducted from Kalamata, Greece, between 30 August and 6 September 2016, and eight flights were conducted from Kathmandu, Nepal, between 27 July and 10 August 2017. Our study mainly adopts a

statistical approach to analyse the entire observational data set comprising measurements from all flights. Figure 1 shows all flight tracks and their positions relative to the typical ASM anticyclone area for the two respective years determined using the criterion defined below in Seciton 2.3.2.. The Kalamata base in 2016 was located outside the ASM anticyclone and air inside or exported from the ASM anticyclone was only probed sporadically. The Kathmandu base in 2017 was located inside the ASM anticyclone region and according to the criterion used (Section 2.3.2.), the bulk of the observations were made within the ASM anticyclone. A comprehensive campaign overview and descriptions of the purpose and specific meteorological situation for each flight are given by Stroh et al. (2020).

2.2 Measurements, dynamical coordinates and analysis tools

2.2.1 Carbon Monoxide (CO)

Carbon monoxide was measured by the new AMICA (Airborne Mid Infrared Cavity enhanced Absorption spectrometer) instrument deployed for the first time during StratoClim. AMICA consists of a power module and a pressurized enclosure containing all major optical components and data acquisition hardware. The instrument is placed underneath a dome-shaped structure on top of the Geophysica aircraft, drawing air from a rear facing inlet through a 2-m length of SilcoNert[®] coated stainless steel tubing. It employs the ICOS (Integrated Cavity Output Spectroscopy, O'Keefe et al., 1999) technique to measure the trace gases Carbonyl Sulfide (OCS), Carbon Dioxide (CO_2), water vapour (H_2O) and CO in the wavenumber range $2050.25 – 2051.1$ cm^{-1}. Full instrumental details will be given in a forthcoming paper (Kloss et al., 2020).

CO mixing ratios were retrieved from observed infrared spectra using a transition at 2050.90 cm^{-1} with line parameters taken from the HITRAN 2012 database (Rothman et al., 2013) and no further calibration parameters. The accuracy was cross-checked for a range of mixing ratios (30 – 5000 ppb) prepared from a 5 ± 0.05 ppm CO standard (AirProducts) by dilution with nitrogen or argon (argon was used at the lowest mixing ratios because the nitrogen gas bottle contained a CO impurity at a concentration of ~30 ppb). Taking into account uncertainty in the standard and uncertainties in the mass flow controller (MFC) flows used to dilute it, the overall accuracy is estimated to be better than 5%. For our analysis, we use AMICA CO data at 10-second time resolution. These data have a 1-sigma precision of ~20 ppb, determined mainly by electrical noise in the observed spectra. Individual CO profiles from all flights are provided in Figure S1 in the supplementary material.

2.2.2 Ozone (O_3)

O_3 was measured with 8 % precision at 1 Hz time resolution by the FOZAN-II (Fast OZone ANalyzer) instrument developed and operated by the Central Aerological Observatory, Russia, and Institute of Atmospheric Science and Climate, Italy (Ulanovsky et al., 2001; Yushkov et al., 1999). FOZAN-II is a two-channel solid state chemiluminescent instrument featur-

ing a sensor based on Coumarin 307 dye on a cellulose-acetate-based substrate, and is equipped with a high accuracy ozone generator for periodic calibration of each channel every 15 minutes during the flight, ensuring an accuracy better than 10 ppb in the observations. The measured concentration range is $10 - 500$ μg m^{-3}, operating temperature range is -95 to +40°C, and the operating pressure range is $1100 - 30$ mbar (about $0 - 22$ km). The instrument was calibrated at the ground before and after each flight by means of an ozone generator and reference ultraviolet (UV)-absorption O_3 monitor (Dasibi 1008-PC).

Ozone data are available from two of the three Kalamata flights in 2016 and from six of the eight Kathmandu flights in 2017. Individual O_3 profiles from all flights are provided in Figure S2 in the supplement.

2.2.3 Nitrous Oxide (N_2O)

N_2O was measured at 90 s time resolution with an average precision of 0.5% and average accuracy of about 0.6% by the High Altitude Gas Analyzer (HAGAR). The instrument, operated by the University of Wuppertal, comprises a 2-channel gas chromatograph with electron capture detection (ECD) measuring a suite of long-lived tracers (N_2O, CFC-11, CFC-12, Halon-1211, CH_4, SF_6, H_2) and a non-dispersive IR absorption sensor for fast CO_2 measurements (Homan et al., 2010). The instrument is calibrated every 7.5 min during flight with either of two standard gases, which are inter-calibrated in the laboratory with standards provided by NOAA/GML (National Oceanic and Atmospheric Administration/Global Monitoring Laboratory). N_2O data are available for all flights of the campaign (note that the first flight on August 30, 2016 in Kalamata suffers from comparatively poor N_2O precision of ~2%).

N_2O is fairly well-mixed in the troposphere with a global mean surface mole fraction in 2017 of 329.8 ppb; its tropospheric distribution exhibits a steady growth of 0.9 ppb a^{-1}, as well as seasonal variation, interhemispheric difference and other geographic variations (on the order of 1 ppb) due to surface sources (Dlugokencky et al., 2018; https://www.esrl.noaa.gov/gmd/hats/combined/N2O.html). N_2O is destroyed in the mid stratosphere mainly above 25 km by UV light and reaction with O(^{1}D), with slow vertical transport to this sink region resulting in a long atmospheric lifetime of 123 (104-152) years (SPARC, 2013). For an air parcel in the lower stratosphere, an N_2O mixing ratio below the tropospheric value thus indicates the presence of a fraction of photochemically aged air that has passed the sink region above.

2.2.4 Geolocation and meteorological data

Temperature was measured at 10 Hz resolution with an accuracy of 0.5 K and a precision of 0.1 K by the commercial Rosemount probe instrument TDC. Pressure and geolocation data were obtained at 1 Hz resolution from the Geophysica's avionic system. Potential temperature along the flight track was calculated from these data. Physical properties on larger scales were derived from ECMWF ERA-Interim data (Dee et al., 2011), including wind speed and direction, potential vorticity (PV),

vertical velocities and radiative heating, and local temperature profiles to determine the heights of the lapse rate tropopause (LRT) and cold point tropopause (CPT).

The vertical resolution of ERA-Interim data in the tropopause region is about 1 km, with relevant levels at 132.76, 113.42, 95.98, 80.40, and 66.62 hPa (corresponding to about 14.23, 15.33, 16.50, 17.74, and 19.05 km). Related to this vertical reso-
175   lution is an uncertainty in the determination of the tropopause level. The space-time variability of the tropopause over the campaign region and period will be assessed from its standard deviation in the following.

2.3 Dynamical Coordinates

2.3.1 Potential temperature relative to the tropopause

180   Key question Q3 (Section 1) addresses how the ASM vertical transport relates to the tropopause. Based on the temperature profile (note that the tropopause is sometimes also defined in terms of other parameters such as PV or chemical tracers), the tropopause in the ASM region can be defined either as the CPT, i.e. the altitude of the coldest temperature, or as the LRT, i.e. "*the lowest level at which the lapse rate decreases to 2 K/km or less, provided also the average lapse rate between this level and all higher levels within 2 km does not exceed 2 K/km*" (WMO, 1957). LRT and CPT were linearly interpolated to
185   each point along a given flight track from the surrounding reanalysis grid points. Under tropical conditions, in the majority of the cases the LRT and CPT are found at the same level, i.e., the LRT is also CPT. When they are not co-located, by definition the CPT is always higher than the LRT, and their separation typically increases with latitude (Munchak and Pan, 2014, see also Figure S3 in the supplementary material, which shows the LRT – CPT separation along the StratoClim flight tracks as a function of latitude).

190   Because both the LRT and the CPT can vary substantially in altitude, potential temperature, and PV, we determine the respective difference in potential temperature units for our observations and introduce this difference as a new vertical coordinate (e.g. Hoor et al., 2004; Ploeger et al., 2017). Pan et al. (2018) have shown that the LRT better identifies the transition from the troposphere to the stratosphere in the tropics, and relative coordinates with respect to the LRT are used in the main figures and discussions below. Corresponding figures with respect to the CPT are provided in the supplementary material to
195   facilitate comparison with studies having a stronger focus on the CPT. For example, Brunamonti et al. (2018) used the CPT to mark the top of an "Asian tropopause transition layer (ATTL)".

2.3.2 Monsoon equivalent latitude

Different meteorological variables have been proposed in the literature to identify the core of the ASM circulation, including geopotential height (e.g. Bergman et al., 2013; Randel and Park, 2006), Montgomery stream function (e.g. Santee et al.,

200 2017) and (e.g. Garny and Randel, 2013; Ploeger et al., 2015). All of these approaches give meaningful (and similar) results when applied to monthly mean fields. Here, we follow the approach of Ploeger et al. (2015) based on the maximum PV gradient on an isentropic surface with respect to a monsoon-centred equivalent latitude (see below). As PV is an approximately conserved quantity it correlates better with tracer distributions that involve small-scale structures, an advantageous quality when applied to high-resolution in-situ measurements.

205 Monsoon equivalent latitude (MeqLat) was introduced by Ploeger et al. (2015, please refer to this reference for a comprehensive description of the MeqLat concept and its derivation) as a means of describing the position of an air mass relative to the centre of the ASM anticyclone. On the 380 K potential temperature surface, the location of the absolute PV minimum is defined as the ASM centre corresponding to 90° MeqLat. As one moves away from this "ASM pole", MeqLat decreases as PV increases. The area enclosed by a given PV contour determines the corresponding MeqLat value, analogous to the de-

210 crease in latitude when moving away from the Earth's north or south pole in the definition of equivalent latitude as proposed by Nash et al. (1996). The anticyclone border (i.e. the transport barrier separating air masses inside and outside) is characterized by a maximum of the PV-gradient with respect to MeqLat and typically lies around 65° MeqLat, so that MeqLat > 65° can be considered as an indicator of air inside the ASM anticyclone (Ploeger et al., 2015). This boundary identification based on the PV gradient only works well in a shallow layer around 380 K. Therefore we use the 380 K MeqLat value at the hori-

215 zontal location of each measurement to determine whether it was made inside or outside the ASM anticyclone. By definition, this criterion is exact only for observations at 380 K and becomes increasingly uncertain with vertical distance above or below this level because the anticyclone varies in size at different levels it often tilts northward with altitude. However, it is the best we can do based on PV. This uncertainty in the correct identification of ASM anticyclone air masses has probably little effect on our analyses of observations around the tropopause level (i.e. around 380 K), but the impact could be more signifi-

220 cant at higher levels where more observations unrelated to the ASM may potentially be included in our analyses. Figure S4 in the supplementary material shows maps of ASM anticyclone frequency for 2016 and 2017 analogous to that shown for 2011 by Ploeger et al. (2015).

2.4 Whole Atmosphere Community Climate Model (WACCM)

The Whole-Atmosphere Community Climate Model, version 6 (WACCM6, Gettelman et al., 2019) is used in this study to

225 provide large-scale dynamical and chemical background for the StratoClim campaign period. WACCM6 is the atmospheric

component of the Community Earth System Model Version 2 (CESM2, Danabasoglu et al., 2020; Emmons et al., 2020). The WACCM6 domain extends from the Earth's surface to the lower thermosphere. For the simulation used in this study, the model uses a 0.9° x 1.2° longitude-latitude grid, with 110 vertical levels on a hybrid-pressure vertical grid with a top at about 150 km (Garcia and Richter, 2019). For pressures < 100 hPa, the vertical coordinate is isobaric; at higher pressures the coor-

230 dinate is hybrid, transitioning to pure terrain following at the surface. The vertical resolution in the UTLS is ~ 0.5 km. WACCM6 uses comprehensive troposphere, stratosphere, mesosphere and lower thermosphere chemistry (TSMLT, Gettel-man et al., 2019). Anthropogenic emissions are from the global CAMS (Copernicus Atmosphere Monitoring Service) emission data set version 4, downloaded from the ECCARD data page: www.igacproject.org/sites/default/files/2018-03/Issue_61_FebMar_2018.pdf. Fire emissions are based on the FINN inventory Version 1.5 (Wiedinmeyer et al., 2011).

235 The WACCM6 simulation used in this study has been performed with observed sea-surface temperature and sea-ice conditions. Atmospheric winds and temperatures are nudged towards NASA GMAO GEOS5.12 meteorological analysis with a Newtonian relaxation of 50 hours below 50 km using a smooth transition to no nudging at higher model levels from 50 to 60 km. The main effect of nudging is to provide meteorological conditions that are consistent with analysed winds and temperature, allowing comparisons between WACCM6 and observed chemical distributions.

240 As the first application of this 110 level configuration in observational studies, we find that the representation of the UTLS dynamical structure of the ASM anticyclone and the region of active convective uplifting are both qualitatively consistent with the result of the previous 88 level configuration, which was extensively analyzed in Pan et al. (2016). The representation of enhanced CO in the anticyclone is also found qualitatively consistent with the MLS satellite data. There is a clear improvement in this run compared to the previous 88 level configuration in a much better representation of the vertical

245 chemical gradient in the UTLS (see Figure 5 in Section 3.3.) The overall performance of this run in representing various process is still under evaluation, especially the possible weaker convective uplifting introduced by the change in nudging.

3 Observations

3.1 General overview

Figure 2 gives a full 3-dimensional view of the AMICA CO observations made during both StratoClim campaigns. The data

250 have been averaged into 1°×1°×1 km longitude/latitude/altitude grid cells, and then meridional and zonal averages have been projected into longitude-altitude and latitude-altitude space. In the Kalamata region, CO mixing ratios in the free troposphere were typically between 50 and 80 ppb and only reached 100 ppb in the lowermost 3 km, with the latter likely due to upward mixing of local boundary layer air. By contrast, measurements in the free troposphere over Nepal and surrounding

regions indicate elevated levels of CO around 100 ppb at altitudes up to about 16 km, in some cases 17 km, i.e. throughout most of the free troposphere. These relatively large CO mixing ratios indicate fast and efficient transport – most likely by convection – from the boundary layer up to this level (see discussion below). Note that the convective activity was weak to moderate during the first half of the 2017 Kathmandu campaign phase and strongly increased in the second half, coinciding with a cooling of the ASM anticyclone and a corresponding rise of θ isentropes in terms of altitude (Bucci et al., 2020; Stroh et al., 2020, and references therein). For a large-scale perspective of the ASM region during the Kathmandu 2017 campaign, animations of WACCM-simulated CO distributions are provided as a supplement (https://doi.org/10.5446/48163).

ERA-Interim reanalysis data show that, at the time of the 2016 campaign, Kalamata was located almost exactly at the border between the tropics and extratropics, defined here as the latitude where the LRT drops sharply from 16 – 18 km in the tropics to 10 – 13 km at higher latitudes (this also shows itself by the sharp PV gradient on the 380 K isentrope in the campaign area displayed in the top panel of Figure 1, and in the strong increase of potential temperature difference between LRT and cold point displayed in Figure S3). As a consequence, air masses in the tropical UTLS and in the extratropical stratosphere were probed in the same altitude range (15 – 20 km), often during the same flight. Air masses sampled in the extratropical strato­sphere show a clear signature of aged stratospheric air, with small CO mixing ratios in the 10 to 25 ppb range. Such air masses were not sampled in the Kathmandu area, where the LRT was always located above 16 km altitude and 369 K poten­tial temperature.

3.2 Trace gas distributions

In Figure 3, campaign-averaged CO, O_3 and N_2O mixing ratios are shown against different horizontal and vertical coordi­nates. In the top row, where data are shown in latitude – potential temperature space, average LRT and CPT levels are also shown for different latitudes. Both levels are highly variable, especially in the (higher latitude) Kalamata region. To account for this variability when separating mixing ratio data into tropospheric and stratospheric regimes, the middle row of Figure 3 adopts θ units relative to the LRT as the new vertical coordinate (defined in Section 2.3.1). A similar figure using the differ­ence in theta relative to the CPT is provided in the supplement (Figure S6). The clear separation between the Kalamata and Kathmandu flights in latitude space becomes less pronounced in the bottom row, where the latitude coordinate is replaced by MeqLat (see Section 2.3.2) to better represent measurement locations relative to the ASM (with MeqLat = 90° being, by definition, at the centre of the ASM anticyclone). Nevertheless, observations obtained during the Kathmandu flights repre­sent most of the data at larger MeqLat values.

Based on Ploeger et al. (2015), we use 65° MeqLat as the boundary between inside the ASMA and outside the ASMA. This must be regarded as an approximation, because this boundary is not always sharp and readily located and can also vary over

time (Ploeger et al., 2015). Moreover, defining the boundary on the 380 K isentropic surface introduces ambiguities for measurements collected at significantly higher or lower levels (see Section 2.3.2). An illustration of this problem is the cluster of samples with 40 – 70 ppb CO just below 350 K in Figure 4 that were observed in the free troposphere over the Mediterranean during the Kalamata campaign (cf. Figure S1).

To further investigate the vertical structure inside the ASM anticyclone, layer-normalized frequency distributions of the three trace gases for all observations collected inside the anticyclone (i.e. with MeqLat > 65 °) are shown in Figure 4 for the vertical coordinates θ (top panels) and Δθ relative to the LRT (bottom panels; a version with potential temperature relative to the CPT is provided in Supplementary Figure S7). Tropospheric CO mixing ratios of around 100 ppb, a clear signature of polluted air, stretch upward from the PBL through the lower troposphere up to about 370 K potential temperature corresponding to about 10 – 20 K below the LRT. The mean LRT during the campaign period is located at about 380 K, with maximum values up to 396 K and minimum values down to 369 K (see Fig. 4). The mean CPT level is located about 10 K higher. Note that potential temperature is highly perturbed in this active convective region and that there is a particularly sharp vertical gradient in theta around the LRT, with a 10 K theta difference corresponding to only a few hundred meters in altitude. Above the LRT, CO mixing ratios > 100 ppb were not observed in these measurements. Above the 360 – 370 K level, CO gradually decreases with altitude until reaching stratospheric equilibrium values of 25 ppb or lower between 420 and 435 K. The observed CO decrease with increasing theta is consistent with the expected local photochemical removal during slow ascent: almost all observations fall into the purple shaded region in the top left panel of Figure 4, which marks realistic combinations of ascent rate and CO lifetime. Isentropic ascent rates between 1.0 and 1.5 K day^{-1} are consistent with ERA-interim based analyses in recent studies (e.g. Garny and Randel, 2016; Legras and Bucci, 2020; Vogel et al., 2019). The reduction of the lower limit to 0.7 K day^{-1} is based on the assumption that ERA interim ascent rates in the monsoon region could be similarly high biased as has been suggested for the TTL (e.g., Ploeger et al., 2012; Schoeberl et al., 2012). The range of 30 – 90 days for the CO photochemical lifetime is conservatively chosen to encompass a wide range of mainly tropospheric lifetime estimates (e.g. Holloway et al., 2000, Xiao et al., 2007, Duncan et al., 2007) and account for the fact that OH concentration decreases with altitude. Note that the WACCM simulation (Section 2.4) predicts CO lifetimes of ~ 1 month at 150 hPa and 1 – 2 months at 100 hPa.

Ozone, as a stratospheric tracer, behaves opposite to CO. Below about 365 K, O_3 mixing ratios mostly fall into the 30 – 50 ppb range and never exceed 100 ppb, consistent with expectations for tropospheric air. A significant increase in O_3 with increasing altitude was observed above this level. As with the decrease in CO, this increase in O_3 is largely consistent with local photochemical production during slow ascent. The purple shaded region in the top middle panel of Figure 4 is based on the same vertical ascent rates described for CO above O_3 production rates of about 4 ppb day^{-1} based on Fig. 8 in Gottschaldt

et al. (2017). Above about 420 K, observed O_3 is higher, probably due to significant in-mixing of stratospheric air above this level, consistent with significant reductions in N_2O mixing ratios (cf. below).

315 A noteworthy feature in Figure 4 is that the gradual decrease in CO and the gradual increase in O_3 show no obvious discontinuities, on average, at the LRT or CPT. However, during the StratoClim campaign the LRT marked the vertical limit above which even individual occurrences of CO > 100 ppb were not observed (Figure 4, bottom left panel).

N_2O measurements are used to assess the role of in-mixing of stratospheric air at different levels. The local tropospheric N_2O mixing ratio is determined by averaging all observations below 360 K potential temperature, which yields a value of 332.7 ±
320 1.7 ppb. We then examine the decrease in N_2O with increasing altitude above this level (Figures 3 and 4). Significant reductions in N_2O mixing ratios (unambiguously indicating significant stratospheric in-mixing) were observed only above about 395 K potential temperature and for $\Delta\theta$ more than 15 K above the mean LRT. Between 400 and 410 K, these reductions become more substantial and a clear decline with increasing potential temperature is visible above this level. From the N_2O measurements, we can estimate the fraction of aged extratropical air entrained into the anticyclone at 400 K, following the
325 approach of Homan et al. (2010; there estimating the extratropical fraction of tropical transition layer, TTL, air). Defining 'aged' here as residing in the stratosphere longer than the lifetime of CO, we select as 'aged' parcels those with CO < 37 ppb (~1/e times the tropospheric CO value of 100 ppb) from the 2016 Kalamata campaign outside the anticyclone, which exhibit a mean N_2O mixing ratio of 320 ± 3.7 ppb (1 standard deviation) in the potential temperature range 390 to 400K. Considering the upper end of the N_2O range and allowing for a 1 ppb increase between 2016 and 2017, we estimate $N_2O_{aged} < 324.7$
330 ppb, i.e. at least 8 ppb below the mean tropospheric value in the Kathmandu region (332.7 ppb). Inside the anticyclone at 400K potential temperature, the average N_2O decreased by only 2.4 ppb from this tropospheric value, consistent with an average fraction of in-mixed aged air of at most 30% (i.e. 2.4 ppb / 8ppb).

3.3 CO – O_3 tracer correlations

Mixing is an important physical process impacting the transport of chemical constituents and a key mechanism for irreversi-
335 ble stratosphere-troposphere exchange (Gettelman et al., 2011). Signatures of mixing in the tropopause region are frequently observed as "mixing lines" in (non-linear) correlations between tropospheric (like CO) and stratospheric (like O_3) tracers (e.g. Marcy et al., 2004; Hoor et al., 2002; Fischer et al., 2000; Hintsa et al., 1998). Thus, mixing layers separating the troposphere from the overlying stratosphere are marked by relatively high concentrations of both CO and O_3. This mixing itself manifests in the CO–O_3 phase space as deviations from the pure tropospheric and pure stratospheric branches, which in the
340 absence of mixing tend to form an L-shaped distribution (Pan et al., 2010; Pan et al., 2007). Such idealized L-shaped CO–O_3

correlations have been used many times to illustrate near-perfect segregation of the troposphere and stratosphere without any mixing layer in between (e.g. Konopka and Pan, 2012).

Figure 5 shows CO–O_3 correlation plots of all coincident CO and O_3 observations from the Kathmandu 2017 flights (left) and from WACCM (right; CO–O_3 mixing ratios in the WACCM distributions are the model outputs from the grid locations closest to the observations in both time and space). Observed CO–O_3 correlations show neither an ideal L-shape nor distinct mixing lines between the tropospheric and stratospheric branches. Rather, there is a smooth curved transition from the tropospheric CO branch to the stratospheric O_3 branch with increasing theta, consistent with a transition layer in which the ascending air undergoes photochemical processing. This interpretation is supported by quasi-coincident N_2O observations largely showing near-tropospheric values in the transition zone between the high-CO tropospheric branch and the high-O_3 stratospheric branch (Figure 5 inset). The points circled in red in Figure 5 (observed during both ascent and descent near Kathmandu during a flight on 31 July) are speculatively associated with fresh convective outflow, for which O_3 mixing ratios are somewhat elevated due to lightning NO_x.

The spatial distribution of the CO–O_3 pairs in the transition layer (dashed magenta rectangle in Figure 5) is shown in Figure 6 by using altitude, pressure and potential temperature as the vertical coordinate (from left to right, respectively). From these distributions, we deduce a vertical extent of the transition layer (Figure 6) with respect to these coordinates of ~16 – 19 km, ~70 – 115 hPa and ~365 – 415 K. Figure 5 also shows that the lower tropospheric end of the transition layer is clearly located below the LRT and the higher stratospheric end is located above the LRT. A more detailed analysis of LRT and CPT locations within the transition layer is given in Figure 7. Observed CO–O_3 pairs with transition layer characteristics are found mainly between 15 K below and 35 K above the local LRT (a few very rare outliers are even found up to 45 K above the LRT), with roughly one third of the pairs found below and two thirds above the LRT. Transition layer CO–O_3 pairs are observed mainly between 30 K below and 30 K above the CPT, with roughly two thirds below and one third above the CPT.

Compact CO–O_3 correlations were also observed during the START08 campaign, during which air masses originating from the tropical tropopause layer (TTL) were sampled in the extratropical UTLS region (Vogel et al., 2011, their Fig. 3). Similar to our observations within the anticyclone, photochemical processing within the observed air masses outweighed mixing effects. They attributed this result to the long transit times associated with air mass transport from tropical convective outflow to the upper part of the TTL, well above the LZRH, which allows time for gradual changes in the CO–O_3 correlation. The relatively fast isentropic transport from the upper part of the TTL to the extra-tropics where the START08 flights took place is less crucial.

Overall, WACCM represents the measured correlations well. The curved part of the correlation representing the transition layer is clearly visible, and the simulation closely matches observations with respect to CO–O_3 coordinates as well as corre-

sponding potential temperature levels. The overall correlation is somewhat more compact in the model compared to the observations. The spread of stratospheric CO measurements from AMICA is about 20 ppbv, which is consistent with the reported measurement precision (see Section 2.2.1); by contrast, WACCM CO shows hardly any spread. In addition to the effect of the relatively coarse model grid size, this compactness might reflect the fact the model does not represent all sources of natural variability (e.g., it does not calculate explicitly the local effects of small-scale gravity waves).

4 Discussion

We now address questions Q1 – Q4 formulated in Section 1 based on the results presented in Section 3. In each subsection below, we discuss one question individually. A refined overall picture of vertical transport in the ASMA region near the tropopause is then given in Section 5.

4.1 Rapid convective transport

Our results provide clear evidence of chimney-like vertical transport from the boundary layer to the tropopause over Nepal and northern India, where almost the entire troposphere shows CO mixing ratios similar to those in the polluted boundary layer. Such high CO mixing ratios are consistently observed up to 360 K, often up to 370 K and occasionally up to 380 K. The absence of observed CO mixing ratios close to or above 100 ppb at levels above 380 K indicates that we did not observe any occurrences of convective outflow above the tropopause immediately prior to the measurement time. However, after mixing with the local background following transport to this level, signatures of deep convection in CO and O_3 are expected to be small and may therefore not be apparent, so we cannot exclude the occurrence of rapid convective uplift reaching up to or even above the tropopause based on our observations. Nevertheless, the absence of significant N_2O reductions below 400 K (Section 3.2) and the shape of the CO–O_3 correlations, with little indication for direct mixing between the tropospheric and stratospheric branches (Section 3.3), reveal that the chemical composition in the 370 – 400 K region cannot be explained by very deep convection mixing with aged stratospheric air. Rather, overshoots penetrating the tropopause mix into the tropospheric air slowly rising out of the 360 – 370 K main convective outflow layer. Our observations provide clear evidence that this slow upwelling (discussed in Section 4.2) and not overshooting convection is the major pathway for air crossing the tropopause in the ASM anticyclone and that the fast chimney-like transport related to convection does indeed stop below the tropopause as suggested by Pan et al. (2016), at least on a synoptic scale. It should be noted that this result does not contradict the significance of overshooting convection for species such as H_2O that are subject to microphysical removal at the CPT (e.g. Ueyama et al., 2018), and that evidence for overshooting convection occurring in the StratoClim year has been shown (Legras and Bucci, 2020).

Although our observations support the hypothesis of significant input into the anticyclone from a chimney region centred near the southern flank of the Tibetan Plateau, the campaign did not cover a wide enough region to characterize the relative contributions of convection from other sources based solely on the observations. Recent studies have demonstrated horizontal transport of convective outflow from locations over China into the ASM anticyclone (Lee et al., 2019; Yuan et al., 2019) as well as injections into the ASM anticyclone from tropical typhoons (Li et al., 2017; Li et al., 2020). Evidence for such import into the air masses probed in 2017 has been shown in trajectory studies (Bucci et al., 2020; Lee et al., 2020).

4.2 Transition to slow upwelling

From our observations, we constrain the top of the main convective outflow layer to about 16 km altitude or 370 K potential temperature, although a few occurrences of convective signatures are observed up to 380 K. Above this level, the gradual decline in CO and gradual increase in O_3 suggest continued slow ascent on timescales comparable to those on which CO is photochemically destroyed and O_3 is photochemically produced (Figure 4). This dynamically driven slow upwelling is radiatively balanced and is less geographically confined than the convective uplift. Pure trajectory models show an "upward spiralling motion of air" extending over large parts of the ASM anticyclone (Vogel et al., 2019; Legras and Bucci, 2020).

This picture is consistent with mean diabatic heating rates from the ERA-Interim reanalysis in July and August (Figure 8). Relatively strong total diabatic tendencies exceeding 1 K day^{-1} extend upward into the upper troposphere in the tropical part of the monsoon region, south of ~30°N and east of ~70°E. This diabatic "chimney" results from frequent deep convective activity up to around 370 K, although single convective events may reach higher. Legras and Bucci (2020) show high clouds in 2017 to be mostly distributed between 340 and 370 K, with some rare convective events reaching up to 400 K This is very similar to the cloud top height distribution over the ASM region that was shown for 2007 by Ueyama et al. (2018).

It can be seen in the right panels in Figure 8 that the convective activity extends clearly above the level of zero radiative heating (LZRH). Thus, radiatively-balanced upwelling (Figure 8, middle panels) leads to continued upward motion of the air masses. In ERA-Interim, positive isentropic vertical velocities up to 1.5 K day^{-1} (comparable with upwelling in the "shallow branch" of the Brewer-Dobson Circulation in the tropics, e.g. Wright and Fueglistaler, 2013) are present well above the 380 K level. These rates are consistent with the range used for the purple shading in Figure 4 and thus with the observed CO decline and O_3 production with increasing potential temperature (Figure 4). Note that this is not quantitatively conclusive because the respective photochemical processing rates are only rough estimates. In addition, precise conclusions on upwelling rates may be affected by uncertainties associated with using PV at 380 K to identify inside-anticyclone points (cf. Section 2.3.2). It should also be noted that other reanalysis data sets may yield quantitatively different results (e.g. Wright and Fueglistaler, 2013; Tao et al., 2019).

4.3 Relationship of the transition region with respect to the tropopause

As stated in Section 4.1, our observations show no evidence of convection crossing the tropopause. At respective mean po-
tential temperature levels of 380 K (minimum: 369 K, maximum: 396 K) and 390 K (min: 370 K, max: 411 K), both the
LRT and the CPT are located within the radiative upwelling regime described in Section 4.2. CO mixing ratios in the ASM
anticyclone do not drop any more sharply at the LRT or CPT than in the regions immediately above or below these levels,
and they remain greater than stratospheric background concentrations up to about 40 K above the LRT and 30 K above the
CPT. The absence of any sharp transition implies that neither the LRT nor the CPT represents a vertical transport barrier for
these species (neglecting, for the present discussion, microphysical processes and constituents affected by them), consistent
with earlier studies (e.g.Vogel et al., 2019). That the LRT and CPT are located well below the level of significant strato-
spheric in-mixing (see Section 4.4) implies that these levels do not represent separation between the troposphere and the
stratosphere in the ASM anticyclone in either a dynamical or chemical sense. Thus the "*tropospheric bubble*" (Pan et al.,
2016) not only extends to an exceptionally high tropopause but even above that tropopause.

In the transition layer (~ 365 – 415 K), the air appears to be largely isolated within the ASM anticyclone, which is visible in
the N_2O observations in this study (Section 3.2). The isolation of air has also been reported in other StratoClim studies (e.g.
Brunamonti et al., 2018; Legras and Bucci, 2020) and in previous puiblications (e.g. Randel and Park, 2006; Park et al.,
2007). The higher-than-stratospheric-background CO values in the transition layer, therefore, indicate that vertical cross-
tropopause transport occurred within the ASM region. This type of evidence of vertical transport has also been seen from
previous in situ measurements of water vapor (Bian et al., 2012) and particle profiles (Yu et a., 2017) over the Tibetan plat-
eau. As shown by the CO-O_3 correlations (Fig. 5), WACCM reproduces the smooth transition from tropospheric to strato-
spheric character over a potential temperature range comparable to the observations, encompassing the range of LRT and
CPT.

4.4 In-mixing of stratospheric air

Taking N_2O mixing ratios significantly below the current tropospheric value as an indicator for the contribution of strato-
spheric air (Section 3.2), mixing of the rising ASM air with older stratospheric air starts to become clearly visible at about
400 K potential temperature. Further indication of stratospheric in-mixing are O_3 mixing ratios exceeding the range ex-
plained by local photochemical production above 420 K (Figure 4). CO mixing ratios at 415 K and above largely match the
stratospheric background value (Figure 4 and Section 3.3), indicating that the tropospheric character of the ASM anticyclone
ceases at or below this level. Individual observations of slightly elevated CO are found up to 435 K where, based on the radi-
ative upwelling rates and CO lifetimes discussed in Section 3.2, CO photochemical decay to equilibrium values is expected

to be complete. A contribution of ASM anticyclone air atpotential temperature levels up to 460 K had been demonstrated by Vogel et al. (2019) using a longer lives tracer than CO. The significant isolation of the ASM anticyclone air up to 400 K and the rapid weakening of this isolation in the range between 400 and 435 K shown by our observations is roughly consistent
460 with previous analyses of ASM confinement using trajectory analyses (Randel and Park, 2006; Brunamonti et al., 2018; Legras and Bucci, 2020).

5 Conclusions

In situ observations of CO, O_3 and N_2O were collected during two aircraft campaigns near the edge and near the centre of the ASM anticyclone. CO and N_2O are tropospheric tracers with short and long photochemical lifetimes, respectively, while O_3
465 is a mainly stratospheric tracer. Analysis of these observations helps us to further fill in the emerging picture of vertical transport in the ASM anticyclone, confirming and extending earlier studies:

- A "fast convective chimney" lifts polluted boundary layer air to the ASM upper troposphere, with the main outflow below 370 K. Evidence of this "chimney" occasionally reaches up to the local LRT around 380 K but was not observed above this level (Figures 2, 3, 4 and 6).

470 - Inside the ASM anticyclone, above the level of main convective outflow, upward transport of air continues at slower rates roughly consistent with vertical velocities and heating rates from reanalysis data and on time scales largely consistent with photochemical removal and production of CO and O_3 respectively (Figures 4 and 5). Our results are consistent with the idea of air "spiralling" upward inside the ASMA, as recently described by Vogel et al. (2019).

- Air crosses the tropopause vertically during this radiatively-balanced ascent, with neither the LRT nor the CPT marking
475 sharp discontinuities for gases not affected by microphysics: the "*tropospheric bubble*" (Pan et al., 2016) extends above the tropopause (Figures 4 and 7).

- Below about 400 K, air is to a large extent horizontally isolated within the ASM anticyclone and in-mixing of stratospheric air from outside is not a dominant factor (N_2O in Figure 4).

- There is no evidence for a sharp vertical boundary marking the top of the ASM anticyclone. The isolation starts to weak-
480 en at 400 K and the degree of mixing with surrounding stratospheric air smoothly increases towards higher levels (decreasing N_2O in Figure 4), consistent with what was shown by Vogel et al. (2019). Clear signatures of tropospheric air undergoing slow chemical processing are retained up to at least 415 K (Figures 4 and 6).

This picture corresponds well to that proposed in a study by Ploeger et al. (2017) who postulated that vertical cross-tropopause transport dominates inside the ASM anticyclone, followed by quasi-horizontal transport along isentropes above the tropopause into the tropics and into the NH extratropical stratosphere. It should be noted, however, that while our observations clearly show cross-tropopause transport within the ASM anticyclone, they do not necessarily contradict horizontal export of air at lower levels, which has, in fact, been shown to occur by others (e.g. Legras and Bucci, 2020; Vogel et al., 2019; Yan et al., 2019). The suggested "two-stage" vertical transport regime with fast convective uplift followed by slow radiative upwelling is consistent with recent trajectory analyses presented by Legras and Bucci (2020) and Vogel et al. (2019), who both show that this upwelling is not localized but rather follows a braod spiral over the entire ASM anticyclone domain. Our results are also consistent with the ATTL picture proposed by Brunamonti et al. (2018). As stated in Section 4.1, our picture of slow upwelling dominating vertical transport across the tropopause does not exclude the occurrence of overshooting events (the significance of which has been emphasized by Ueyama et al., 2018, and Legras and Bucci, 2020), so Brunamonti et al.'s interpretation of a shallow layer of enhanced H_2O mixing ratios above the CPT as an indication of overshooting convection crossing the CPT is not in conflict with this picture. Given the ~5 K temperature drop in the ASM anticyclone at the beginning of August described by Brunamonti et al. (2018), the enhanced H_2O could also result from earlier ascent through a warmer CPT. The concept of the Lagrangian cold point rather than the local CPT being the relevant feature in limiting H_2O transport has been described for the TTL by Pan et al. (2019), and it will be interesting to investigate this further with H_2O observations from the two airborne campaigns.

Data availability. All data will soon be accessible via the HALO database at https://halo-db.pa.op.dlr.de/mission/101 . In the meantime, they can be provided by the PIs upon request.

Author contributions. M. von Hobe, F. Plöger, P. Konopka and L. Pan led and devised the analyses. M. von Hobe and C. Kloss provided AMICA CO observations. A. Ulanovsky, V. Yushkov and F. Ravegnani provided FOZAN O_3 observations. C. M. Volk provided HAGAR N_2O observations. D. Kinnison, R. Garcia developed the new WACCM-110L version and S. Tilmes carried out the simulations for this study. S. Honomichel extracted the CO/O_3 correlations from WACCM and prepared all figures related to CO/O_3 correlations as well as the video supplement showing the WACCM simulations over the campaign period. J. Wright calculated heating rates from ERA-Interim and prepared Figure 8. M. von Hobe prepared figures related to the observations and prepared the manuscript with contributions from all co-authors.

Competing intersts. The authors declare that they have no conflict of interest.

Acknowledgements

We would like to thank the MDB team operating the M55 Geophysica aircraft for the successful deployments and their support with instrument integrations and operation as well as provision of avionic data, as well as local airport and ATC staff in Kalamata and Kathmandu for their support. We also thank Johannes Wintel, Valentin Lauther, Thorben Beckert, Emil Gerhardt and Lydia Eppert, who supported HAGAR operations and data analysis, and Nicole Spelten for preparing time synchronized merged files that were used for our analyses. Special thanks to Fred Stroh for the tremendous spadework he put in to actually make the campaigns and flights in these locations possible, and to Colonel Kharki for diplomatic support in Nepal. Campaign planning and logistics as well as the scientific interpretation was largely covered by the StratoClim project funded by the European Community's Seventh Framework Programme (FP7/2007-2013) under grant agreement n° 603557. Additional support for this work was obtained from the German Bundesministerium für Bildung und Forschung (BMBF) under the ROMIC-SPITFIRE project (BMBF-FKZ: 01LG1205), and from a joint research project funded by the National Natural Science Foundation of China (NSFC project number 41761134097) and the German Research Foundation (DFG project number 392169209). The GEOS data used in the WACCM6 run have been provided by the Global Modeling and Assimilation Office (GMAO) at NASA Goddard Space Flight Center through the online data portal in the NASA Center for Climate Simulation. Felix Ploeger was funded by the Helmholtz Association under grant no. VH-NG-1128 (Helmholtz Young Inves-tigators Group A–SPECi). Corinna Kloss was partly funded by the Deutsche Forschungsgemeinschaft (DFG, German Research Foundation) – 409585735. We thank Michelle Santee, an anonymous reviewer, Rolf Müller and Bärbel Vogel for constructive comments on the manuscript that helped to significantly improve this paper.

References

Bergman, J. W., Fierli, F., Jensen, E. J., Honomichl, S., and Pan, L. L.: Boundary layer sources for the Asian anticyclone: Regional contributions to a vertical conduit, J. Geophys. Res. Atmos., 118, 2560-2575, https://doi.org/10.1002/jgrd.50142, 2013.

Bian, J., Pan, L. L., Paulik, L., Vömel, H., Chen, H., and Lu, D.: In situ water vapor and ozone measurements in Lhasa and Kunming during the Asian summer monsoon, Geophys. Res. Lett., 39, L19808, doi:10.1029/2012GL052996, 2012.

Brunamonti, S., Jorge, T., Oelsner, P., Hanumanthu, S., Singh, B. B., Kumar, K. R., Sonbawne, S., Meier, S., Singh, D., Wienhold, F. G., Luo, B. P., Boettcher, M., Poltera, Y., Jauhiainen, H., Kayastha, R., Karmacharya, J., Dirksen, R., Naja, M., Rex, M., Fadnavis, S., and Peter, T.: Balloon-borne measurements of temperature, water vapor, ozone and aerosol backscatter on the southern slopes of the Himalayas during StratoClim 2016-2017, Atmos. Chem. Phys., 18, 15937-15957, https://doi.org/10.5194/acp-18-15937-2018, 2018.

540 Bucci, S., Legras, B., Sellitto, P., D'Amato, F., Viciani, S., Montori, A., Chiarugi, A., Ravegnani, F., Ulanovsky, A., Cairo, F., and Stroh, F.: Deep convective influence on the upper troposphere–lower stratosphere composition in the Asian monsoon anticyclone region: 2017 StratoClim campaign results, Atmos. Chem. Phys., 20, 12193–12210, https://doi.org/10.5194/acp-20-12193-2020, 2020.

Danabasoglu, G., Lamarque, J. F., Bacmeister, J., Bailey, D. A., DuVivier, A. K. Â., Edwards, J., Emmons, L. K., Fasullo,
545 J., Garcia, R., Gettelman, A., Hannay, C., Holland, M. M., Large, W. G., Lauritzen, P. H., Lawrence, D. M., Lenaerts, J. T. M., Lindsay, K., Lipscomb, W. H., Mills, M. J., Neale, R., Oleson, K. W., Otto-Bliesner, B., Phillips, A. S., Sacks, W., Tilmes, S., van Kampenhout, L., Vertenstein, M., Bertini, A., Dennis, J., Deser, C., Fischer, C., Fox-Kemper, B., Kay, J. E., Kinnison, D., Kushner, P. J., Larson, V. E., Long, M. C., Mickelson, S., Moore, J. K., Nienhouse, E., Polvani, L., Rasch, P. J., and Strand, W. G.: The Community Earth System Model Version 2 (CESM2), J. Adv. Modeling Earth Systems, 12,
550 e2019MS001916, https://doi.org/10.1029/2019MS001916, 2020.

Dee, D. P., Uppala, S. M., Simmons, A. J., Berrisford, P., Poli, P., Kobayashi, S., Andrae, U., Balmaseda, M. A., Balsamo, G., Bauer, P., Bechtold, P., Beljaars, A. C. M., van de Berg, L., Bidlot, J., Bormann, N., Delsol, C., Dragani, R., Fuentes, M., Geer, A. J., Haimberger, L., Healy, S. B., Hersbach, H., Holm, E. V., Isaksen, L., Kallberg, P., Kohler, M., Matricardi, M., McNally, A. P., Monge-Sanz, B. M., Morcrette, J. J., Park, B. K., Peubey, C., de Rosnay, P., Tavolato, C., Thepaut, J. N.,
555 and Vitart, F.: The ERA-Interim reanalysis: configuration and performance of the data assimilation system, Quart. J. Royal Meteor. Soc., 137, 553-597, https://doi.org/10.1002/qj.828, 2011.

Dlugokencky, E. J., B.D. Hall, S.A. Montzka, G. Dutton, J. Muhle and J.W. Elkins, Long-lived greenhouse gases, in: State of the Climate in 2017. Bull. Amer. Meteor. Soc., 99, Si–S310, https://doi.org/10.1175/2018BAMSStateoftheClimate.1, 2018.

560 Duncan, B. N., Logan, J. A., Bey, I., Megretskaia, I. A., Yantosca, R. M., Novelli, P. C., Jones, N. B., and Rinsland, C. P.: Global budget of CO, 1988–1997: Source estimates and validation with a global model, J. Geophys. Res., 112, D22301, doi:10.1029/2007JD008459, 2007.

Emmons, L. K., Schwantes, R. H., Orlando, J. J., Tyndall, G., Kinnison, D., Lamarque, J.-F. o., Marsh, D., Mills, M. J., Tilmes, S., Bardeen, C., Buchholz, R. R., Conley, A., Gettelman, A., Garcia, R., Simpson, I., Blake, D. R., Meinardi, S., and
565 Pétron, G.: The Chemistry Mechanism in the Community Earth System Model Version 2 (CESM2), J. Adv. Modeling Earth Systems, 12, e2019MS001882, https://doi.org/10.1029/2019MS001882, 2020.

Filipiak, M. J., Harwood, R. S., Jiang, J. H., Li, Q., Livesey, N. J., Manney, G. L., Read, W. G., Schwartz, M. J., Waters, J. W., and Wu, D. L.: Carbon monoxide measured by the EOS Microwave Limb Sounder on Aura: First results, Geophys. Res. Lett., 32, L14825, https://doi.org/10.1029/2005GL022765, 2005.

570 Fischer, H., Wienhold, F. G., Hoor, P., Bujok, O., Schiller, C., Siegmund, P., Ambaum, M., Scheeren, H. A., and Lelieveld, J.: Tracer correlations in the northern high latitude lowermost stratosphere: Influence of cross-tropopause mass exchange, Geophys. Res. Lett., 27, 97-100, https://doi.org/10.1029/1999GL010879, 2000.

Fu, R., Hu, Y., Wright, J. S., Jiang, J. H., Dickinson, R. E., Chen, M., Filipiak, M., Read, W. G., Waters, J. W., and Wu, D. L.: Short circuit of water vapor and polluted air to the global stratosphere by convective transport over the Tibetan Plateau,
575 Proc. Nat. Acad. Sciences U.S.A., 103, 5664-5669, https://doi.org/10.1073/pnas.0601584103, 2006.

Garcia, R. R., and Richter, J. H.: On the Momentum Budget of the Quasi-Biennial Oscillation in the Whole Atmosphere Community Climate Model, J. Atmos. Sci., 76, 69-87, https://doi.org/10.1175/JAS-D-18-0088.1, 2019.

Garny, H., and Randel, W. J.: Dynamic variability of the Asian monsoon anticyclone observed in potential vorticity and correlations with tracer distributions, J. Geophys. Res. Atmos., 118, 13421-13433, https://doi.org/10.1002/2013JD020908,
580 2013.

Garny, H., and Randel, W. J.: Transport pathways from the Asian monsoon anticyclone to the stratosphere, Atmos. Chem. Phys., 16, 2703-2718, https://doi.org/10.5194/acp-16-2703-2016, 2016.

Gettelman, A., Hoor, P., Pan, L. L., Randel, W. J., Hegglin, M. I., and Birner, T.: The Extratropical Upper Troposphere and Lower Stratosphere, Rev. Geophys., 49, RG3003, https://doi.org/10.1029/2011RG000355, 2011.

585 Gettelman, A., Mills, M. J., Kinnison, D. E., Garcia, R. R., Smith, A. K., Marsh, D. R., Tilmes, S., Vitt, F., Bardeen, C. G., McInerny, J., Liu, H. L., Solomon, S. C., Polvani, L. M., Emmons, L. K., Lamarque, J. F., Richter, J. H., Glanville, A. S., Bacmeister, J. T., Phillips, A. S., Neale, R. B., Simpson, I. R., DuVivier, A. K., Hodzic, A., and Randel, W. J.: The Whole Atmosphere Community Climate Model Version 6 (WACCM6), J. Geophys. Res. Atmos., 124, 12380-12403, https://doi.org/10.1029/2019JD030943, 2019.

590 Gill, A. E.: Some simple solutions for heat-induced tropical circulation, Quart. J. Royal. Meteor. Soc., 106, 447-462, https://doi.org/10.1002/qj.49710644905, 1980.

Gottschaldt, K.-D., Schlager, H., Baumann, R., Bozem, H., Eyring, V., Hoor, P., Joeckel, P., Jurkat, T., Voigt, C., Zahn, A., and Ziereis, H.: Trace gas composition in the Asian summer monsoon anticyclone: a case study based on aircraft observations and model simulations, Atmos. Chem. Phys., 17, 6091-6111, https://doi.org/10.5194/acp-17-6091-2017, 2017.

595 Hintsa, E. J., Boering, K. A., Weinstock, E. M., Anderson, J. G., Gary, B. L., Pfister, L., Daube, B. C., Wofsy, S. C., Loewenstein, M., Podolske, J. R., Margitan, J. J., and Bui, T. P.: Troposphere-to-stratosphere transport in the lowermost stratosphere from measurements of H_2O, CO_2, N_2O and O_3, Geophys. Res. Lett., 25, 2655-2658, https://doi.org/10.1029/98GL01797, 1998.

Holloway, T., Levy, H., and Kasibhatla, P.: Global distribution of carbon monoxide, J. Geophys. Res., 105 (D10), 12123–12147, doi:10.1029/1999JD901173, 2000.

Homan, C. D., Volk, C. M., Kuhn, A. C., Werner, A., Baehr, J., Viciani, S., Ulanovski, A., and Ravegnani, F.: Tracer measurements in the tropical tropopause layer during the AMMA/SCOUT-O3 aircraft campaign, Atmos. Chem. Phys., 10, 3615-3627, https://doi.org/10.5194/acp-10-3615-2010, 2010.

Hoor, P., Fischer, H., Lange, L., Lelieveld, J., and Brunner, D.: Seasonal variations of a mixing layer in the lowermost stratosphere as identified by the CO-O-3 correlation from in situ measurements, J. Geophys. Res., 107, 4044, https://doi.org/10.1029/2000JD000289, 2002.

Hoor, P., Gurk, C., Brunner, D., Hegglin, M. I., Wernli, H., and Fischer, H.: Seasonality and extent of extratropical TST derived from in-situ CO measurements during SPURT, Atmos. Chem. Phys., 4, 1427-1442, https://doi.org/10.5194/acp-4-1427-2004, 2004.

Hoskins, B. J., and Rodwell, M. J.: A Model of the Asian Summer Monsoon. Part I: The Global Scale, J. Atmos. Sci., 52, 1329-1340, https://doi.org/10.1175/1520-0469(1995)052%3C1329:AMOTAS%3E2.0.CO;2, 1995.

Kloss, C., Tan, V., Leen, J. B., Madsen, G. L., Gardner, A., Kulessa, T., Schillings, J., Schneider, J., Schrade, S., and Von Hobe, M.: Airborne Mid-Infrared Cavity enhanced Absorption spectrometer (AMICA), in preparation for Atmos. Meas. Techn., 2020.

Konopka, P., and Pan, L. L.: On the mixing-driven formation of the Extratropical Transition Layer (ExTL), J. Geophys. Res., 117, D18301, https://doi.org/10.1029/2012JD017876, 2012.

Lau, W. K. M., Yuan, C., and Li, Z.: Origin, Maintenance and Variability of the Asian Tropopause Aerosol Layer (ATAL): The Roles of Monsoon Dynamics, Sci. Rep., 8, 3960, https://doi.org/10.1038/s41598-018-22267-z, 2018.

Lee, K. O., Dauhut, T., Chaboureau, J. P., Khaykin, S., Krämer, M., and Rolf, C.: Convective hydration in the tropical tropopause layer during the StratoClim aircraft campaign: pathway of an observed hydration patch, Atmos. Chem. Phys., 19, 11803-11820, https://doi.org/10.5194/acp-19-11803-2019, 2019.

Lee, K. O., Barret, B., Flochmoen, E. L., Tulet, P., Bucci, S., von Hobe, M., Kloss, C., Legras, B., Leriche, M., Sauvage, B., Ravegnani, F., and Ulanovsky, A.: Convective uplift of pollution from the Sichuan basin into the Asian monsoon anticyclone during the StratoClim aircraft campaign, Atmos. Chem. Phys. Discuss., 20, 1-32, https://doi.org/10.5194/acp-2020-581, in review, 2020.

Legras, B., and Bucci, S.: Confinement of air in the Asian monsoon anticyclone and pathways of convective air to the stratosphere during the summer season, Atmos. Chem. Phys., 20, 11045–11064, https://doi.org/10.5194/acp-20-11045-2020, 2020.

Li, D., Vogel, B., Bian, J. C., Müller, R., Pan, L. L., Günther, G., Bai, Z. X., Li, Q., Zhang, J. Q., Fan, Q. J., and Vomel, H.: Impact of typhoons on the composition of the upper troposphere within the Asian summer monsoon anticyclone: the SWOP

630 campaign in Lhasa 2013, Atmos. Chem. Phys., 17, 4657-4672, https://doi.org/10.5194/acp-17-4657-2017, 2017.

Li, D., Vogel, B., Müller, R., Bian, J., Günther, G., Ploeger, F., Li, Q., Zhang, J., Bai, Z., Vömel, H., and Riese, M.: Dehydration and low ozone in the tropopause layer over the Asian monsoon caused by tropical cyclones: Lagrangian transport calculations using ERA-Interim and ERA5 reanalysis data, Atmos. Chem. Phys., 20, 4133-4152, https://doi.org/10.5194/acp-20-4133-2020, 2020.

635 Li, Q., Jiang, J. H., Wu, D. L., Read, W. G., Livesey, N. J., Waters, J. W., Zhang, Y., Wang, B., Filipiak, M. J., Davis, C. P., Turquety, S., Wu, S., Park, R. J., Yantosca, R. M., and Jacob, D. J.: Convective outflow of South Asian pollution: A global CTM simulation compared with EOS MLS observations, Geophys. Res. Lett., 32, L14826, https://doi.org/10.1029/2005gl022762, 2005.

Marcy, T. P., Fahey, D. W., Gao, R. S., Popp, P. J., Richard, E. C., Thompson, T. L., Rosenlof, K. H., Ray, E. A., Salawitch,
640 R. J., Atherton, C. S., Bergmann, D. J., Ridley, B. A., Weinheimer, A. J., Loewenstein, M., Weinstock, E. M., and Mahoney, M. J.: Quantifying stratospheric ozone in the upper troposphere with in situ measurements of HCl, Science, 304, 261-265, https://doi.org/10.1126/science.1093418, 2004.

Munchak, L. A., and Pan, L. L.: Separation of the lapse rate and the cold point tropopauses in the tropics and the resulting impact on cloud top-tropopause relationships, J. Geophys. Res., 119, 7963-7978, https://doi.org/10.1002/2013jd021189,
645 2014.

Nash, E. R., Newman, P. A., Rosenfield, J. E., and Schoeberl, M. R.: An objective determination of the polar vortex using Ertel's potential vorticity, J. Geophys. Res., 101, 9471-9478, https://doi.org/10.1029/96JD00066, 1996.

Nützel, M., Podglajen, A., Garny, H., and Ploeger, F.: Quantification of water vapour transport from the Asian monsoon to the stratosphere, Atmos. Chem. Phys., 19, 8947-8966, https://doi.org/10.5194/acp-19-8947-2019, 2019.

650 O'Keefe, A., Scherer, J. J., and Paul, J. B.: cw Integrated cavity output spectroscopy, Chem. Phys. Lett., 307, 343-349, https://doi.org/10.1016/S0009-2614(99)00547-3, 1999.

Pan, L. L., Bowman, K. P., Shapiro, M., Randel, W. J., Gao, R. S., Campos, T., Davis, C., Schauffler, S., Ridley, B. A., Wei, J. C., and Barnet, C.: Chemical behavior of the tropopause observed during the Stratosphere-Troposphere Analyses of Regional Transport experiment, J. Geophys. Res., 112, D18305, https://doi.org/10.1029/2012JD017695, 2007.

655 Pan, L. L., Bowman, K. P., Atlas, E. L., Wofsy, S. C., Zhang, F. Q., Bresch, J. F., Ridley, B. A., Pittman, J. V., Homeyer, C. R., Romashkin, P., and Cooper, W. A.: The Stratosphere-Troposphere Analyses of Regional Transport 2008 Experiment, Bull. Am. Meteor. Soc., 91, 327-342, https://doi.org/10.1175/2009BAMS2865.1, 2010.

Pan, L. L., Honomichl, S. B., Kinnison, D. E., Abalos, M., Randel, W. J., Bergman, J. W., and Bian, J.: Transport of chemical tracers from the boundary layer to stratosphere associated with the dynamics of the Asian summer monsoon, J. Geophys. Res. Atmos., 121, 14159-14174, https://doi.org/10.1002/2016JD025616, 2016.

Pan, L. L., Honomichl, S. B., Bui, T. V., Thornberry, T., Rollins, A., Hintsa, E., and Jensen, E. J.: Lapse Rate or Cold Point: The Tropical Tropopause Identified by In Situ Trace Gas Measurements, Geophys. Res. Lett., 45, 10756-10763, https://doi.org/10.1029/2018GL079573, 2018.

Pan, L. L., Honomichl, S. B., Thornberry, T., Rollins, A., Bui, T. P., Pfister, L., and Jensen, E. E.: Observational Evidence of Horizontal Transport-Driven Dehydration in the TTL, Geophys. Res. Lett., 46, 7848-7856, https://doi.org/10.1029/2019GL083647, 2019.

Park, M., Randel, W. J., Gettelman, A., Massie, S. T., and Jiang, J. H.: Transport above the Asian summer monsoon anticyclone inferred from Aura Microwave Limb Sounder tracers, J. Geophys. Res., 112, D16309, https://doi.org/10.1029/2006JD008294, 2007.

Park, M., Randel, W. J., Emmons, L. K., Bernath, P. F., Walker, K. A., and Boone, C. D.: Chemical isolation in the Asian monsoon anticyclone observed in Atmospheric Chemistry Experiment (ACE-FTS) data, Atmos. Chem. Phys., 8, 757-764, https://doi.org/10.5194/acp-8-757-2008, 2008.

Park, M., Randel, W. J., Emmons, L. K., and Livesey, N. J.: Transport pathways of carbon monoxide in the Asian summer monsoon diagnosed from Model of Ozone and Related Tracers (MOZART), J. Geophys. Res., 114, D08303, https://doi.org/10.1029/2008JD010621, 2009.

Ploeger, F., Konopka, P., Müller, R., Fueglistaler, S., Schmidt, T., Manners, J. C., Grooß, J.-U., Günther, G., Forster, P. M., and Riese, M.: Horizontal transport affecting trace gas seasonality in the Tropical Tropopause Layer (TTL), J. Geophys. Res., 117, D09303, doi:10.1029/2011JD017267, 2012.

Ploeger, F., Gottschling, C., Griessbach, S., Grooß, J. U., Günther, G., Konopka, P., Müller, R., Riese, M., Stroh, F., Tao, M., Ungermann, J., Vogel, B., and von Hobe, M.: A potential vorticity-based determination of the transport barrier in the Asian summer monsoon anticyclone, Atmos. Chem. Phys., 15, 13145-13159, https://doi.org/10.5194/acp-15-13145-2015, 2015.

Ploeger, F., Konopka, P., Walker, K., and Riese, M.: Quantifying pollution transport from the Asian monsoon anticyclone into the lower stratosphere, Atmos. Chem. Phys., 17, 7055-7066, https://doi.org/10.5194/acp-17-7055-2017, 2017.

Randel, W. J., and Park, M.: Deep convective influence on the Asian summer monsoon anticyclone and associated tracer variability observed with Atmospheric Infrared Sounder (AIRS), J. Geophys. Res., 111, D12314, https://doi.org/10.1029/2005JD006490, 2006.

Randel, W. J., Park, M., Emmons, L., Kinnison, D., Bernath, P., Walker, K. A., Boone, C., and Pumphrey, H.: Asian Monsoon Transport of Pollution to the Stratosphere, Science, 328, 611-613, https://doi.org/10.1126/science.1182274, 2010.

690   Rothman, L. S., Gordon, I. E., Babikov, Y., Barbe, A., Benner, D. C., Bernath, P. F., Birk, M., Bizzocchi, L., Boudon, V., Brown, L. R., Campargue, A., Chance, K., Cohen, E. A., Coudert, L. H., Devi, V. M., Drouin, B. J., Fayt, A., Flaud, J. M., Gamache, R. R., Harrison, J. J., Hartmann, J. M., Hill, C., Hodges, J. T., Jacquemart, D., Jolly, A., Lamouroux, J., Le Roy, R. J., Li, G., Long, D. A., Lyulin, O. M., Mackie, C. J., Massie, S. T., Mikhailenko, S., Muller, H. S. P., Naumenko, O. V., Nikitin, A. V., Orphal, J., Perevalov, V., Perrin, A., Polovtseva, E. R., Richard, C., Smith, M. A. H., Starikova, E., Sung, K.,

695   Tashkun, S., Tennyson, J., Toon, G. C., Tyuterev, V. G., and Wagner, G.: The HITRAN2012 molecular spectroscopic data base, J. Quant. Spec. Rad. Transfer, 130, 4-50, http://dx.doi.org/10.1016/j.jqsrt.2013.07.002, 2013.

Santee, M. L., Manney, G. L., Livesey, N. J., Schwartz, M. J., Neu, J. L., and Read, W. G.: A comprehensive overview of the climatological composition of the Asian summer monsoon anticyclone based on 10 years of Aura Microwave Limb Sounder measurements, J. Geophys. Res. Atmos., 122, 5491-5514, https://doi.org/10.1002/2016JD026408, 2017.

700   Schoeberl, M. R., Dessler, A. E., and Wang, T.: Simulation of stratospheric water vapor and trends using three reanalyses, Atmos. Chem. Phys., 12, 6475–6487, https://doi.org/10.5194/acp-12-6475-2012, 2012.

SPARC Report on the Lifetimes of Stratospheric Ozone-Depleting Substances, Their Replacements, and Related Species, M. Ko, P. Newman, S. Reimann, S. Strahan (Eds.), SPARC Report No. 6, WCRP-15/2013, 2013.

Stroh, F., et. al., e.: First detailed airborne and balloon measurements of microphysical, dynamical and chemical processes in

705   the Asian Summer Monsoon Anticyclone: Overview and First Results of the 2016/17 StratoClim field campaigns, in preparation for Atmos. Chem. Phys., 2020.

Tao, M., Konopka, P., Ploeger, F., Yan, X., Wright, J. S., Diallo, M., Fueglistaler, S., and Riese, M.: Multitimescale variations in modeled stratospheric water vapor derived from three modern reanalysis products, Atmos. Chem. Phys., 19, 6509–6534, https://doi.org/10.5194/acp-19-6509-2019, 2019.

710   Thomason, L. W., and Vernier, J. P.: Improved SAGE II cloud/aerosol categorization and observations of the Asian tropopause aerosol layer: 1989-2005, Atmos. Chem. Phys., 13, 4605-4616, https://doi.org/10.5194/acp-13-4605-2013, 2013.

Ueyama, R., Jensen, E. J., and Pfister, L.: Convective Influence on the Humidity and Clouds in the Tropical Tropopause Layer During Boreal Summer, J. Geophys. Res. Atmos., 123, 7576-7593, https://doi.org/10.1029/2018JD028674, 2018.

Ulanovsky, A. E., Yushkov, V. A., Sitnikov, N. M., and Ravegnani, F.: The FOZAN-II fast-response chemiluminescent air-

715   borne ozone analyzer, Instruments and Experimental Techniques, 44, 249-256, 2001.

Vernier, J. P., Thomason, L. W., and Kar, J.: CALIPSO detection of an Asian tropopause aerosol layer, Geophys. Res. Lett., 38, 2011.

Vogel, B., Pan, L. L., Konopka, P., Günther, G., Müller, R., Hall, W., Campos, T., Pollack, I., Weinheimer, A., Wei, J., Atlas, E. L., and Bowman, K. P.: Transport pathways and signatures of mixing in the extratropical tropopause region derived from Lagrangian model simulations, J. Geophys. Res., 116, 2011.

Vogel, B., Günther, G., Müller, R., Grooß, J. U., and Riese, M.: Impact of different Asian source regions on the composition of the Asian monsoon anticyclone and of the extratropical lowermost stratosphere, Atmos. Chem. Phys., 15, 13699-13716, 2015.

Vogel, B., Müller, R., Günther, G., Spang, R., Hanumanthu, S., Li, D., Riese, M., and Stiller, G. P.: Lagrangian simulations of the transport of young air masses to the top of the Asian monsoon anticyclone and into the tropical pipe, Atmos. Chem. Phys., 19, 6007-6034, https://doi.org/10.5194/acp-19-6007-2019, 2019.

Wiedinmyer, C., Akagi, S. K., Yokelson, R. J., Emmons, L. K., Al-Saadi, J. A., Orlando, J. J., and Soja, A. J.: The Fire INventory from NCAR (FINN): a high resolution global model to estimate the emissions from open burning, Geosci. Model Dev., 4, 625-641, https://doi.org/10.5194/gmd-4-625-2011, 2011.

WMO: Meteorology - A three dimensional science: Second session of the Commission for Aerology, WMO Bulletin, IV(4), 134-138, 1957.

Wright, J. S. and Fueglistaler, S.: Large differences in reanalyses of diabatic heating in the tropical upper troposphere and lower stratosphere, Atmos. Chem. Phys., 13, 9565–9576, https://doi.org/10.5194/acp-13-9565-2013, 2013.

Xiao, Y. P., Jacob, D. J., and Turquety, S.: Atmospheric acetylene and its relationship with CO as an indicator of air mass age, J. Geophys. Res.-Atmos., 112, 2007.

Yan, X., Konopka, P., Ploeger, F., Podglajen, A., Wright, J. S., Müller, R., and Riese, M.: The efficiency of transport into the stratosphere via the Asian and North American summer monsoon circulations, Atmos. Chem. Phys., 19, 15629-15649, 2019.

Yu, P., Rosenlof, K. H., Liu, S., Telg, H., Thornberry, T. D., Rollins, A. W., Portmann, R. W., Bai, Z., Ray, E. A., Duan, Y., Pan, L. L., Toon, O. B., Bian, J., and Gao, R.-S.: Efficient transport of tropospheric aerosol into the stratosphere via the Asian summer monsoon anticyclone, Proc. Nat. Acad. Sciences U.S.A., 114, 6972-6977, 2017.

Yuan, C., Lau, W. K. M., Li, Z., and Cribb, M.: Relationship between Asian monsoon strength and transport of surface aerosols to the Asian Tropopause Aerosol Layer (ATAL): interannual variability and decadal changes, Atmos. Chem. Phys., 19, 1901-1913, 2019.

Yushkov, V., Oulanovsky, A., Lechenuk, N., Roudakov, I., Arshinov, K., Tikhonov, F., Stefanutti, L., Ravegnani, F., Bonafe, U., and Georgiadis, T.: A chemiluminescent analyzer for stratospheric measurements of the ozone concentration (FOZAN), Journal of Atmospheric and Oceanic Technology, 16, 1345-1350, 1999.

Figures
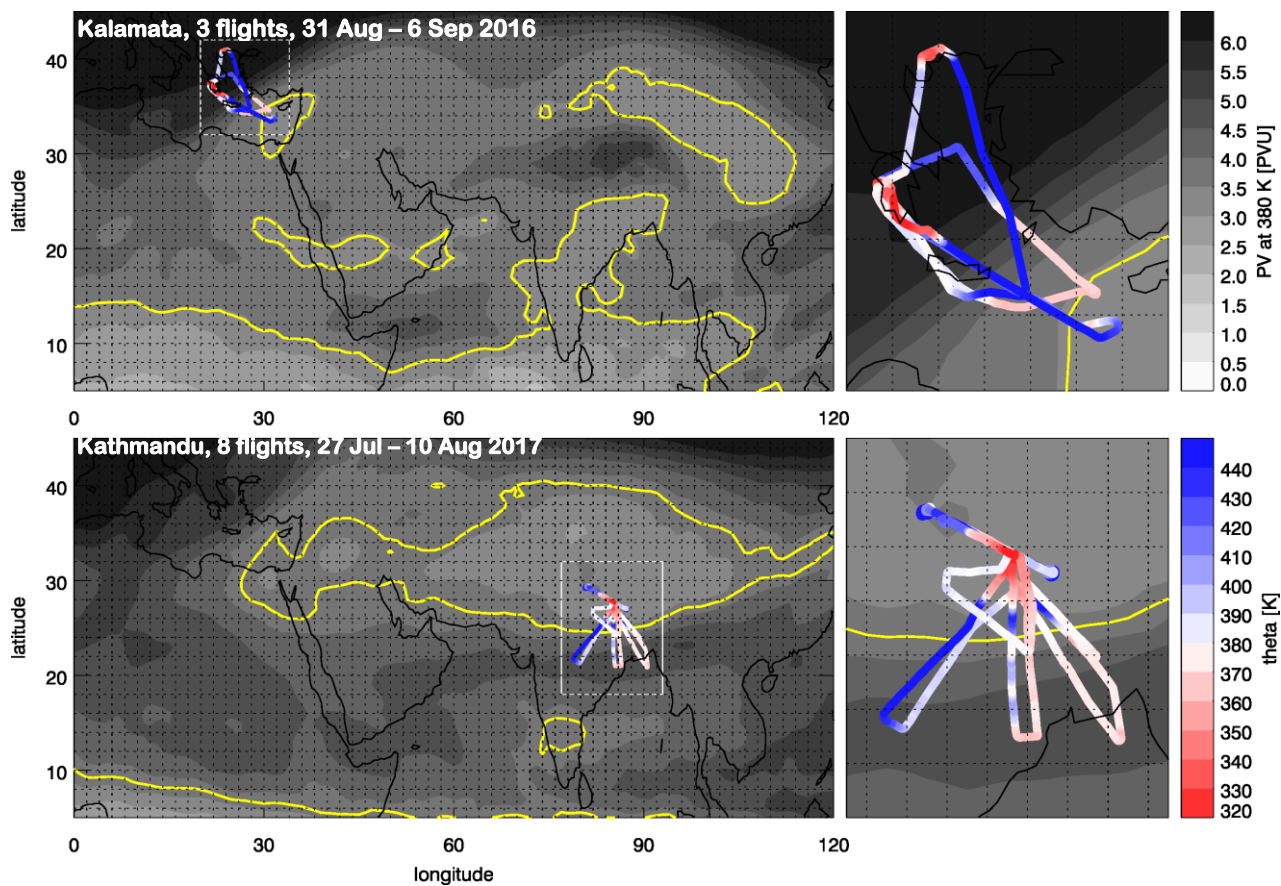
Figure 1 Maps showing tracks of all Geophysica flights conducted during the StratoClim campaign phases in 2016 (top) and 2017 (bottom) for the larger ASM area (left) and zoomed to the respective campaign area (right). PV contours (grey shadings),averaged between 29 Aug and 7 Sep 2016 and between 26 Jul and 11 Aug 2017 respectively, are shown for the 380 K potential temperature level, on which the Ploeger et al. (2015) criterion is applied to determine the average ASM anticyclone boundaries for the two campaign periods (yellow lines; PV thresholds were determined to be 3.5 PVU for 2016 and 3.7 PVU for 2017; maps of the average ASM anticyclone position for the full monsoon season, i.e. 1 July – 31 August, are shown in Supplementary Figure S4).
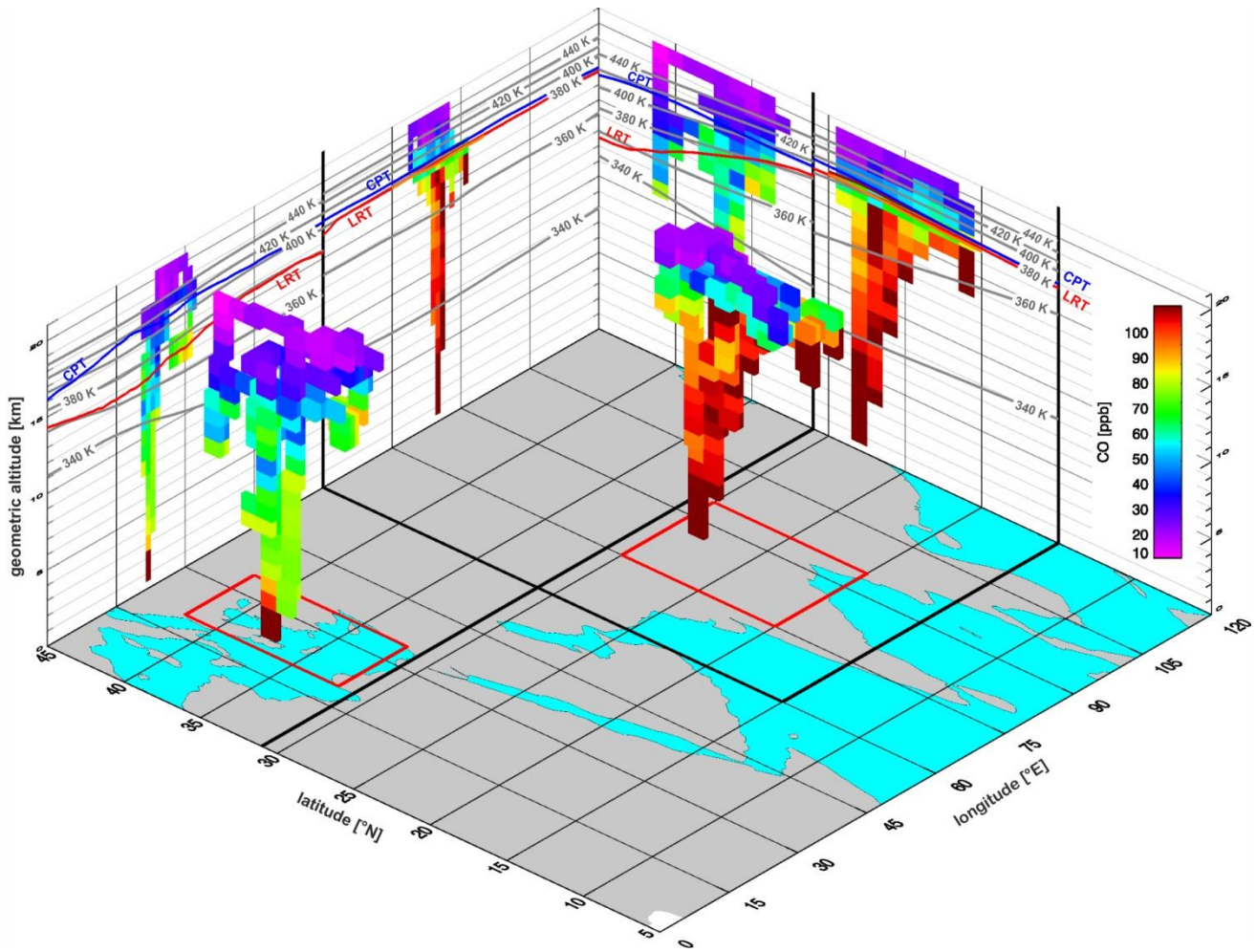
Figure 2 3D Map of averaged CO mixing ratios observed during all StratoClim flights (raw CO profiles for all individual flights are
765 shown in supplementary Figure S1). Values in 3D space represent averages in $1° \times 1° \times 1$ km longitude – latitude – altitude bins.
Longitude-altitude averages over all latitudes and latitude-altitude averages over all longitudes are projected onto the x-z and y-z
planes respectively. Grey contour lines in the x-z and y-z planes show potential temperature levels averaged meridionally and zonally
over the areas marked on the map by the thick black lines; red and blue lines show LRT and CPT heights averaged over the same
areas (based on ERA-Interim reanalysis products during the respective campaign phases).
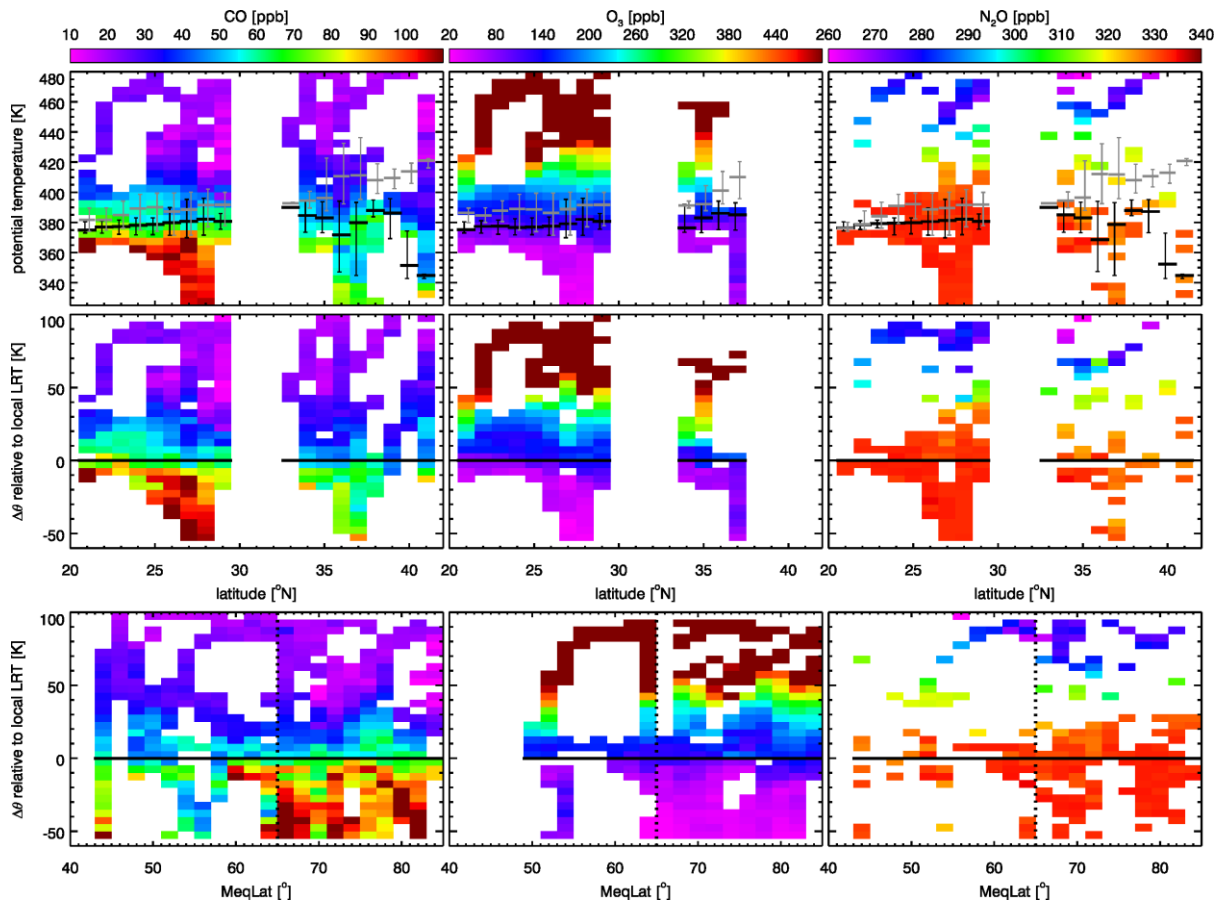
Figure 3 Top panels show CO (left), O$_3$ (middle) and N$_2$O (right) mixing ratios averaged from both deployments into 1° latitude × 5 K potential temperature bins. Black and grey bars show average and minimum/maximum LRT and CPT heights respectively for all measurements made in each 1° latitude bin. Note that the bins with valid data for CO, O$_3$ and N$_2$O do not exactly match due to different data coverage for the AMICA, FOZAN and HAGAR instruments. The middle panels show the same data with potential temperature relative to the LRT (see Section 2.3.1) as the vertical coordinate. In the bottom panels, the horizontal coordinate is transformed to MeqLat with the vertical dotted line marking the 65° ASM anticyclone boundary (see Section 2.3.2). The number of samples and standard deviation in each bin are given in Figure S5 in the supplementary material.
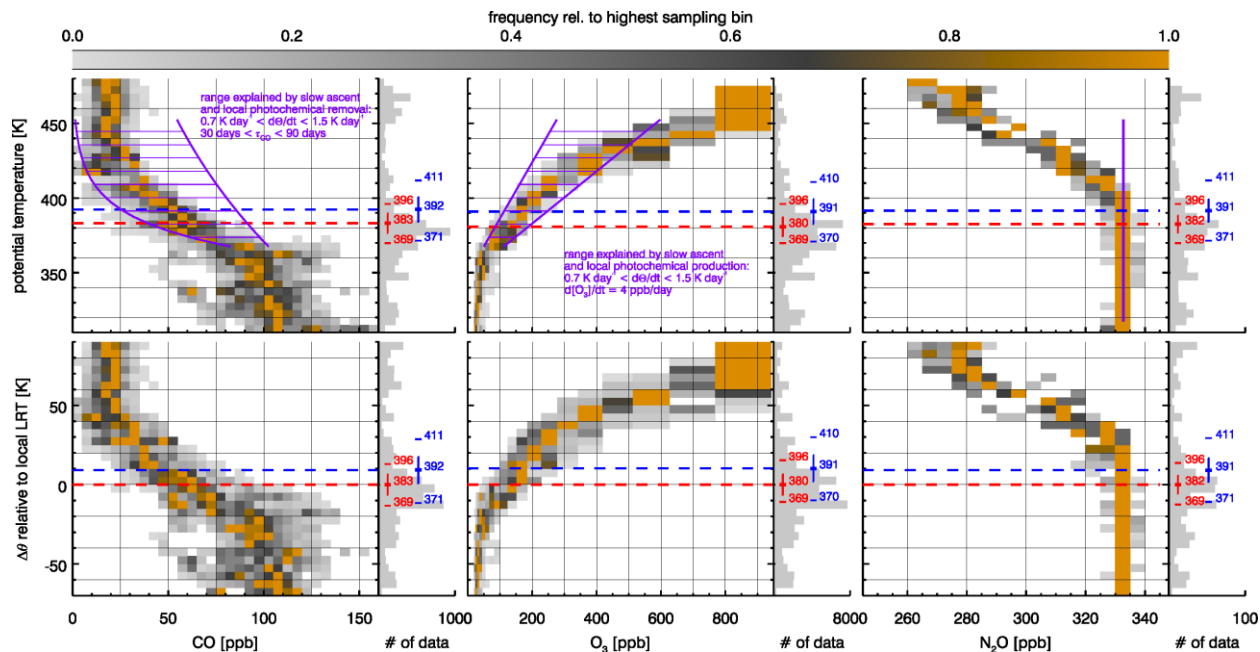
Figure 4 Layer-normalized relative frequency distributions of CO (left), O_3 (middle) and N_2O (right) inside the ASM anticyclone (MeqLat > 65 °) for vertical coordinates of potential temperature (top) and potential temperature difference relative to the local LRT (bottom). The number of observations on each vertical level is plotted as the grey histogram along the right side of each panel (scaling from 0 to the number at the right end of the axis). The mean (with standard deviation), minimum and maximum LRT and CPT levels are also shown in red and blue, respectively (values vary slightly between the columns because, as explained in the Fig. 3 caption, the bins with valid measurements are different for each instrument). Areas marked in purple in the CO and O_3 panels indicate the range of concentrations consistent with photochemical removal/production during slow ascent (see text for the rationale behind the chosen ranges). In the N_2O panel, the purple line denotes the average HAGAR N_2O in the troposphere (below 360 K potential temperature) during the 2017 campaign.
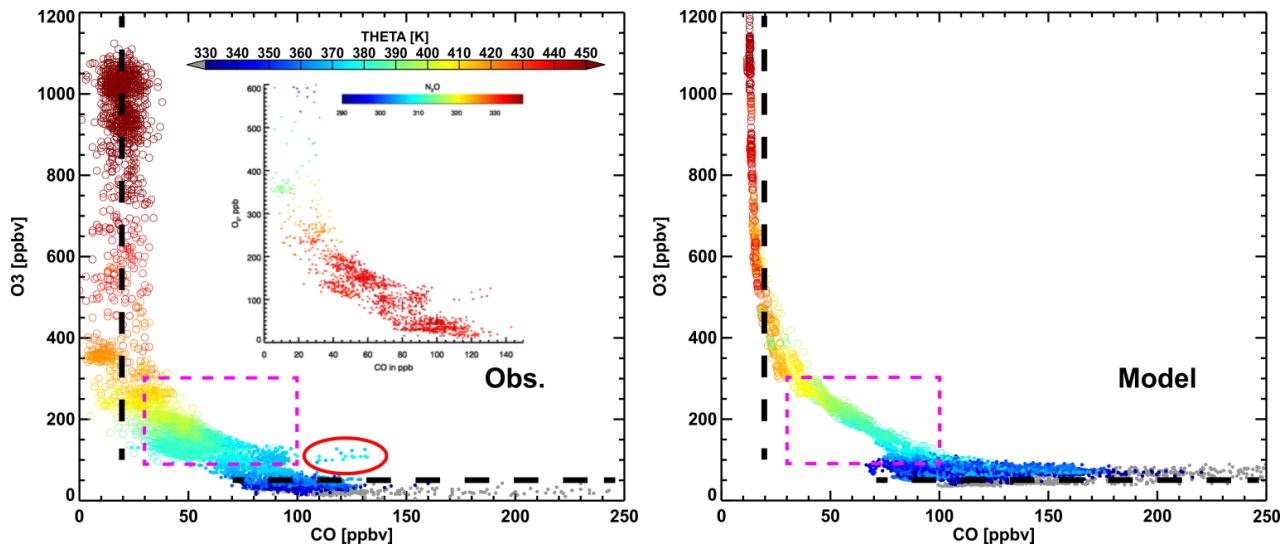
Figure 5 O_3 vs CO relationships in tracer-tracer space based on observations (left) and WACCM simulations (right) for the 2017 Kathmandu flights. The data points are coloured according to their potential temperature level (with grey indicating $\theta < 330$ K) and they are shown by two types of symbols for above (circle) and below (dots) the LRT. WACCM grid points are selected to match the flight dates and are sampled in grid points nearest to the flight track (within $\pm 1°$ in latitude and longitude) to minimize space-time offsets. Dashed lines indicate three "regimes" identified by the O_3-CO relationship, corresponding to the troposphere (horizontal dashed line), the stratosphere (vertical dashed line) and the transition layer (magenta rectangle). We chose criteria of 30 ppb < CO < 100 ppb and 80 ppb < O_3 < 300 ppb to assign measurements to the transition layer (i.e. both gases having neither tropospheric nor stratospheric values). The points marked by the red oval are likely produced by convective transport and O_3 production from lightning NOx (see text). The inset in the left panel shows the observed O_3 vs. CO relationship coloured according to quasi-simultaneous N_2O observations (points are only displayed if the time of measurement is within 30 seconds of a HAGAR N_2O measurement, and if the difference in theta at the times of CO/O_3 and N_2O measurements is less than 2.5 K).
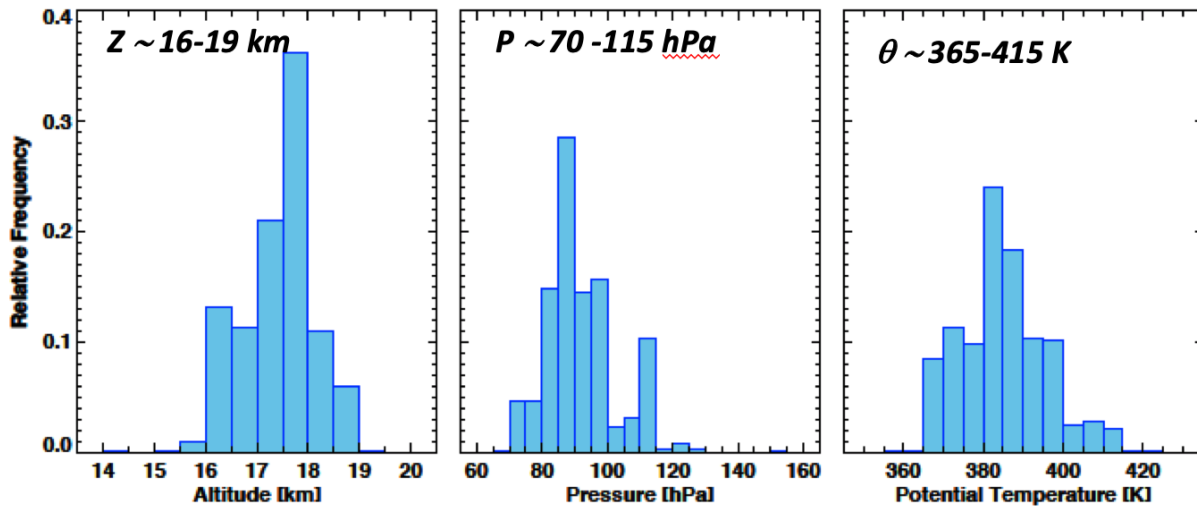
Figure 6 Relative frequency distributions of transition-layer measurements in altitude, pressure, and θ coordinates.
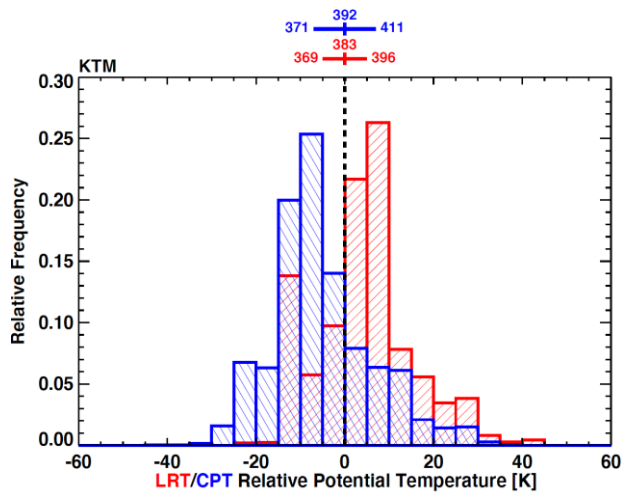
Figure 7 Transition layer in tropopause-relative potential temperature coordinates. Histograms show normalized relative frequency distributions of transition layer measurements as defined in the text. The distribution relative to the LRT (CPT) is shown in red (blue). The mean and the range of the LRT and CPT in potential temperature coordinates (as shown in Figure 4) are given in matching colours above the zero line.
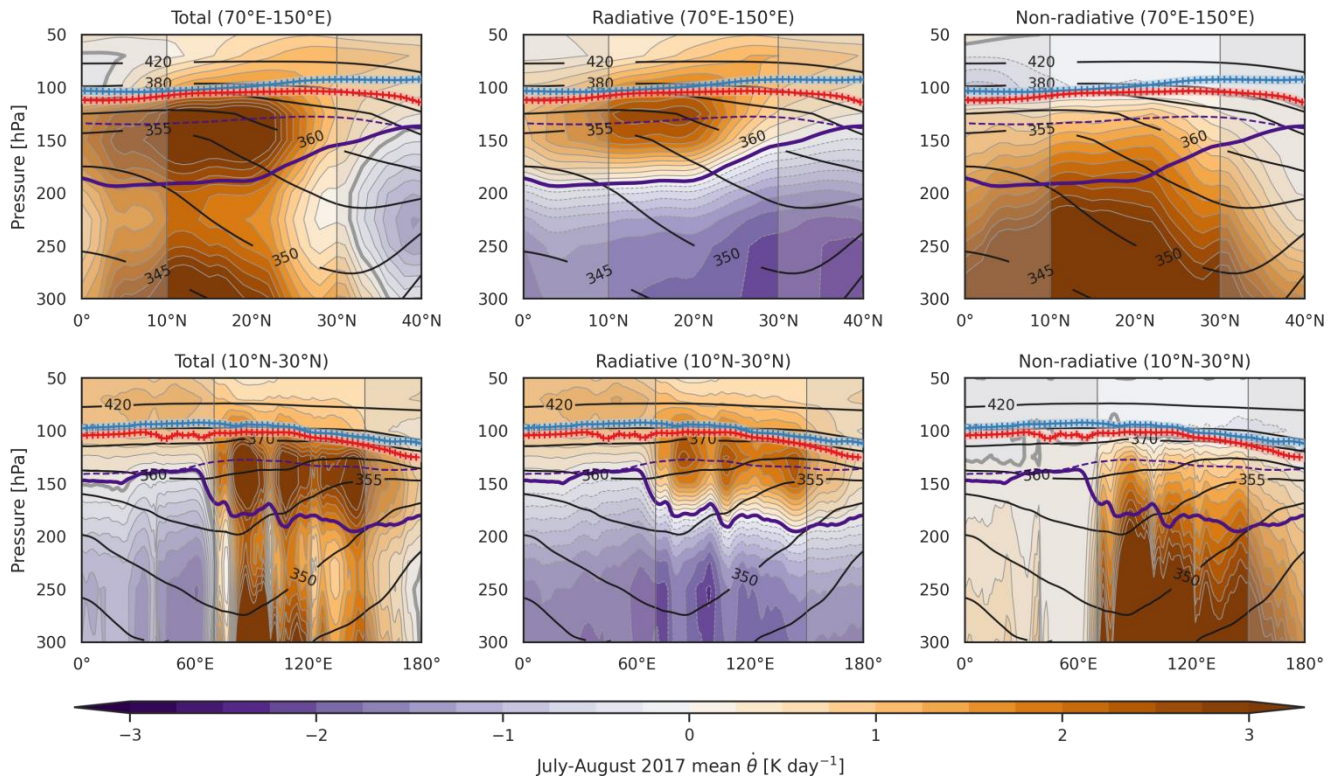
Figure 8 Zonally (top) and meridionally (bottom) averaged total (left), radiative (centre) and non-radiative (right) diabatic potential temperature tendencies (dθ/dt)_diab based on the ERA-Interim reanalysis for July-August 2017. As demarcated by the vertical grey lines and bolder colors on the respective panels, zonal averages are calculated over 70 – 150°E and meridional averages over 10 – 30°N with area weights applied. Black contours show potential temperature. Purple contours show the vertical location of the LZRH based on the zero contour in time-mean radiative heating rates under all-sky (solid) and clear-sky (dashed) conditions. LRT and CPT are shown in red and blue respectively. Averaging ranges for θ contours, LZRH, LRT and CPT are the same as those for (dθ/dt)_diab.